Manipulation of Individual Magnetic Domain Walls with a Local Circular Field

XIAOLIN HU

Laboratory of Professor Katherine Aidala

Physics Department

Mount Holyoke College

South Hadley, Massachusetts

May 2012

I give permission for public access to my thesis for any copying to be done at the discretion of the archives librarian and/or the College librarian.

Signature: _____ Date: _____

Acknowledgment

I am heartily thankful to the following people for this thesis would not be possible without their encouragement, guidance and support:

♢ My advisor Katherine Elizabeth Aidala for introducing me to the intriguing nano world. She has inspired me in every possible way a woman student in science can be inspired.

♢ Dr. Nihar Pradhan, Dr. Huajie Ke and Dr. Tianyu Yang for their patient and generous help with fabrication and experiments. While busy searching jobs or finishing theses, they spend hours and days training me, working with me and trading off measurements.

♢ Professor Mark Peterson and Professor Maria Gomez for willing to sit on my committee.

♢ Professor Roberto Salgato for willing to mentor me during my first summer. Professor Janice Hudgings to mentor me for a one-year independent study in Optics. Her passion for research aspires me to become a future researcher.

♢ My labmates from both Aidala and Janice group: San, Susu, Ruimin, Qinxia, Pawana, Hexuan, Clare, Abby, Alyssa, Amy, Kadhir, Joyce and Jason. Thank you for sharing the joy and bearing with my random "depression" along the way.

♢ Leon and Thomas for making new setups and fixing old ones.

♢ Physics department for being extremely supportive and maintaining such a comfortable lounge.

♢ My family and my friends for supporting me in various ways and wikipediaing domain walls and AFM.

Thank You!

Abstract

Understanding domain wall (DW) motion in nanoscale ferromagnetic structures reveals intriguing physics, with tremendous potential applications in logic devices and racetrack memory. Work has been done to move a series of DWs uniformly, either by passing spin-polarized currents or applying non-uniform magnetic fields. One challenge remained is to create and move individual DWs in arbitrary locations. We developed a technique to generate localized circular magnetic field by applying a current through the tip of the atomic force microscope (AFM) and thereby manipulating the state of the ferromagnetic rings[1, 2]. Now we extend our ability to control domain walls in various structures, such as straight wires with notches and zigzag wires. By placing the tip near a 180° DW in a vertex of a zigzag wire, we can move the 180° DW along the wire and form a stable 360° DW in neighboring vertex. We can also separate the 360° DW back to two 180° DWs or annihilate the 360° DW entirely. Micromagnetic simulations have been performed at Odyssey computer cluster at Harvard University with Object Oriented Micro Magnetic Framework (OOMMF), a public domain program distributed by NIST, to study the evolution of magnetic states in various structures in a uniform or circular magnetic field. NiFe and Co nanowires have been fabricated with Electron Beam Lithography and lift-off technique. We are presently working on to experimentally pass current through AFM tip and examine magnetic states with Magnetic Force Microscope (MFM) imaging. In the future, we plan to simultaneously measure magnetoresistance while manipulating DWs in order to monitor the motion while it is occurring. We would also like to understand the probabilistic nature of DW motion in a greater depth.

Table of Contents

1 Introduction to Magnetism **11**

1.1 Electrons and Magnetic Moments 12

1.2 Origin of Ferromagnetism 13

1.3 Micromagnetic Energy 14

1.3.1 Exchange Energy 14

1.3.2 Demagnetization Energy 15

1.3.3 Anisotropy Energy 16

1.3.4 Zeeman Energy 18

1.4 Domain Wall Formation 19

2 Motivation and Previous Work **22**

2.1 Ferromagnetic Nanowires 23

2.2 Racetrack Memory 25

2.3 Present Methods to Control Domain Walls 28

2.4 Domain Wall Manipulation in a Local Magnetic Field 31

3 Computational Methods **34**

3.1 Overview of Simulation Procedure 35

3.2 LLG equation derivation 37

4 Experimental Methods **42**

4.1 Sample Fabrication 43

4.2 Atomic Force Microscopy 48

4.3 Magnetic Force Microscopy 51

4.4 Variable Field Module 54

4.5 Creating a Local Circular Field 55

5 Results **57**

5.1 Zigzag Nanowires 58
5.1.1 Simulation 59
5.1.2 Experiment 68
5.2 Curved Nanowires 72
5.2.1 Simulation 72
5.2.2 Experiment 76
5.3 Notched Nanowires 79
5.3.1 Simulation 79
5.3.2 Experiment 80

6 Discussion and Conclusion 84
6.1 Practical Considerations 85
6.1.1 Sample Fabrication 85
6.1.2 Applying Currents at Multiple Locations in Sequence 87
6.1.3 Cell Size Consideration 89
6.2 Stochastic Domain Wall Motion 90
6.3 Magnetoresistance Measurement 92
6.4 Conclusion 93

A Procedures to Apply Local Fields 94

List of Figures

1.1 Magnetic configuration of ferromagnets without and with domain walls. To minimize the total free energy, magnets break into domains with magnetization pointing in different directions. 19

2.1 Evolution of magnetic configurations of zigzag nanowires in an external field in y-direction. The magnetic moments rotate from pointing upward to pointing along the arms, forming domain walls at vertices. 23

2.2 Evolution of magnetic configurations of zigzag nanowires in an external field in x-direction. The magnetic moments rotate from pointing toward right to pointing along the arms continuously. There are no domain walls. 24

2.3 Detailed structures of domain walls near one notch of a wire. The wire is delineated with the white line, 10 nm thick and 200 nm wide. There are a series of notches placed at equal distances apart along the wire. This structure is fabricated at IBM Almaden Center in S.P. Parkin's group [3]. 26

2.4 (a) and (e) show an individual racetrack and a racetrack array. (c) and (d) show the read head and the write head, respectively [3]. 27

2.5 Two domain walls move simultaneously from right to left. The cartoon at top shows a schematic of the experiment. Experimental results are shown for a 40-nm-thick, 100-nm-wide permalloy nanowire with 11 triangular notches located 1 μm apart. Single current pulses, 8V (26 mA) and 14 ns long, were applied between each image sequentially from top to bottom [3]. 28

2.6 Two domain walls move simultaneously from left to right under non-uniform fields. (a) shows the two fields applied between 0 to 1 s and 1 to 2 s, respectively. (b) to (d) show the snapshots of the wire at 0, 1, 2s in the field [4]. 29

2.7 (a) Cartoon shows the experimental set-up for passing current through AFM tips. (b)The IV curve corresponds to a 100 Ω resistance in the circuit [2]. 31

2.8 Magnetic states of nanorings before and after currents are passed. Rings have outer diameter 1200 nm, inner diameter 900 nm. Ring 2 ends in the vortex state, where both walls annihilate. Ring 4 shows that the walls have moved but not annihilate [2]. 32

3.1 A magnetic moment precesses around the magnetic field$\vec{B}$ forever without damping at a constant angle. In reality, the moment eventually aligns to a certain direction. 39

4.1 The cross-section of the sample through out the fabrication. (a) Spin coating (b) E-beam writing and development(c) Metal deposition (d) Lift-off. 43

4.2 Schematic graph showing major component of a typical electron beam evaporator. The electrons are ejected from a tungsten filament. The electrons hit the target material (NiFe/Co) so that the material evaporates onto the substrate due to the heat [5]. 44
4.3 Block diagram showing the major component of a typical e-beam writer [6]. 45
4.4 Major component of an AFM machine [7]. 48
4.5 (a) Cartoon shows the experimental set-up for passing current through AFM tips. (b)The IV curve corresponds to a 100 Ohm resistance in the circuit. 55

5.1 Nanowires of different geometries 58
5.2 Initialization of a zigzag wire in magnetic fields in the y-direction. 60
5.3 Moving a 180° DW with a 25 mA clockwise field. 62
5.4 Separating the 360° DW with a 40 mA clockwise field in wires with widths (a)-(c) 100 nm, (d) 300 nm and (e) 500 nm. 65
5.5 Annihilating a 180° DW with a 40 mA counter-clockwise field. 66
5.6 Injecting 360° DWs with a 40 mA counter-clockwise field in the (a) middle vertex (b) middle of an arm. 67
5.7 AFM image of a typical zigzag nanowire sample. 68
5.8 MFM images of a zigzag nanowire in uniform magnetic fields in y-direction. 69
5.9 We typically pass currents near the head-do-head and tail-to-tail DWs of zigzag nanowires. 70
5.10 MFM images before and after a current is passed. 70

5.11 Magnetization of a curved nanowire after a strong field in the y-direction is applied and removed. 72
5.12 Motion of multiple domain walls in a curved nanowire after 25 mA is passed. Head-to-head DWs are labeled with red bars and tail-to-tail DWs are labeled with blue bars. The green lines indicate the magnetic fields due to the 25 mA current. 75
5.13 AFM image of a typical curved nanowire sample: 77
5.14 MFM image of curved nanowires. It does not change after currents are applied near the 180° DWs. 77
5.15 MFM image of two nanowires after currents are passed. No change is observed right after the current passing process, but DWs move around after the sample is left for a night. . 78
5.16 Evolution of micromagnetic configuration of a notched nanowire in the in-plane field in the y-direction. 79
5.17 DW injection near the notch. 80
5.18 AFM image of a typical notched wire sample. 81
5.19 MFM image of notched nanowires. It does not change after currents are applied near the notches. 82

6.1 Zoomed-in AFM image of a typical notched wire sample . . 86
6.2 Zoomed-in MFM image of a typical notched wire sample. . 86
6.3 Motion of multiple domain walls in a curved nanowire after 25 mA is passed first in the middle corner and then near DW 5. Head-to-head DWs are labeled with red bars and tail-to-tail DWs are labeled with blue bars. The green lines indicate the magnetic fields due to the 25 mA current. . . . 88

6.4 Samples to study field-driven depinning of DW trapped at a notch [10]. 90

6.5 Depinning field distribution for each type of notched wires. The wires are 50 nm thick [10]. 91

A.1 Adjust imaging mode of AFM. 94

A.2 Adjust imaging mode of AFM. 95

A.3 Bring up the tip voltage. 96

A.4 Select the location to pass current. 96

A.5 Adjust the crosspoint setting. 98

A.6 The IV curve of a successful current passing. 99

1. Introduction to Magnetism

This chapter provides the background physics to think about magnetic structures. I will first introduce magnetic moments and spins. I will continue to explain how different energy terms interact to determine the ordering of spins. I will conclude with the discussion of domain wall formation in ferromagnetic materials. I will provide the motivation of my project and a review of previous works in chapter 2.

1.1 Electrons and Magnetic Moments

The physical fundamental unit of magnetism is the magnetic moment m. On the atomic scale, the magnetic moments in solids are associated with the electronic angular momentum, which results from orbital motion and spin. If we think of electrons as particles moving around the nucleus in a circular path due to Coulomb force, we can picture this motion as a current loop around the nucleus, which is equivalent to a magnet according to Ampere's Law. The moment is

$$m = \frac{-e}{2m_e} l \tag{1.1}$$

where e is the electron charge, m_e is the electron mass, and l is the orbital angular momentum.

Electrons also possess a quantum mechanical property, the *spin*, which is associated with an intrinsic magnetic moment. The spin moment can adopt two orientations, spin up or spin down. The magnetic moment is

$$m = \frac{-e}{m_e} s \tag{1.2}$$

where s is the spin momentum. The orbital and spin moments are further coupled to create a total atomic magnetic moment.

1.2 Origin of Ferromagnetism

Atomic magnetic moments interact with each other and respond to the external field in different ways. They collectively determine the material's magnetic property. If the material's atoms have completely filled electron shells, the atomic net spin moment is zero as spin-up and spin-down electrons are paired up and cancel each other out.

If the material's atoms have partially filled electrons, some electrons are left unpaired, leading to net spin moments. In some materials, this results in ferromagnetism, where the material will exhibit a strong net magnetization without an external field. The nearby moments can interact through exchange energy, which I will explain further in following sections. The main point is that in ferromagnets, exchange energy favors parallel alignments of magnetic moments. Examples for ferromagnetic materials are iron (Fe), cobalt (Co) and nickel (Ni). When ferromagnetic materials reach a certain temperature, which is called Curie temperature, thermal fluctuation becomes dominant, spin moments point randomly, and the net magnetic moment is zero. The Curie temperature is material dependent in ferromagnets, and is usually considerably higher than room temperature.

1.3 Micromagnetic Energy

The configuration of magnetic moments is determined by the minimization of the total free energy. The total energy is given by

$$U_{total} = U_{exchange} + U_{demagnetization} + U_{anisotropy} + U_{zeeman} \tag{1.3}$$

It is critical to understand the exchange, demagnetization, anisotropy and Zeeman energies to study ferromagnetic nanostructures. These four terms are explained in details in following sections.

1.3.1 Exchange Energy

The exchange energy for a pair of neighboring spins is represented by a Hamiltonian formed by Heisenberg. We can sum up the exchange energies between all pair of spins across the sample, and get the total exchange energy

$$\hat{H} = -2J \sum_{i>j} S_i \cdot S_j \tag{1.4}$$

where J is the exchange constant, and i and j are indices of spins. The quantum mechanical effect of exchange leads to either parallel or anti-parallel alignment of spins. For positive J, energy is minimized when neighboring spins are parallel; for negative J, energy is minimized when neighboring spins are anti-parallel. Ferromagnetic material has positive J and favors parallel spin configuration. It promotes smooth variation of spin moments and inhibits rapid fluctuation of moments throughout the magnet. This smooth variation is characterized by the exchange length, typically around 3 nm, which provides a sense of the size scale over which moments will be aligned with one another.

1.3.2 Demagnetization Energy

The demagnetization energy is lowest when the demagnetization field is minimized. The magnetic field strength, $\vec{H}$-field is defined as

$$\vec{H} = \frac{\vec{B}}{\mu_0} - \vec{M} \tag{1.5}$$

where $\vec{B}$ is the magnetic flux density, and $\vec{M}$ is the magnetic moment per volume, or *Magnetization*, and μ_0 is the vacuum permeability. Maxwell states that the $\vec{B}$-field is divergenceless,

$$\nabla \cdot \vec{B} = 0 \tag{1.6}$$

Therefore, we have

$$\nabla \cdot \vec{H} = -\nabla \cdot \vec{M} \tag{1.7}$$

Two sources contribute to this self-induced $\vec{H}$-field: the conduction current and the magnetization distribution of the magnet. When no conduction current is present, we can write$\vec{H}$ as $\vec{H}_{demag}$. Within the material, the demagnetization field $\vec{H}_{demag}$ is always opposite to the magnetization. We can write down the demagnetization field as

$$H_{demag,i} = -\vec{N}_{ij} \cdot \vec{M}_j \qquad i,j = x,y,z \tag{1.8}$$

where $\vec{N}_{ij}$ is the demagnetizing tensor, represented by a symmetric 3×3 matrix. At boundary of the material, $\vec{M}$ ends abruptly, resulting in a stray magnetic field $\vec{H}_{demag}$ outside the material. The total energy can be calculated by integrating magnetic energy over all space,

$$U_{demagnetization} = \frac{1}{2} \int \mu_0 \vec{H}^2_{demag} \, d^3r \tag{1.9}$$

And it is clear that the demagnetization energy is lowest when $\vec{H}_{demag}$-field is minimized.

1.3.3 Anisotropy Energy

Magnetic anisotropy describes the tendency of magnetization to lie along some particular easy axis. The anisotropy energy can be written as

$$U_{anisotropy} = K_u \sin^2 \theta \tag{1.10}$$

where θ is the angle between $\vec{M}$ and easy axis, and$K_u$is anisotropy constant, measured in Jm^3 .

As we are considering thin-film structures, we mainly take into account two sources of anisotropy. The first is shape anisotropy, which results from the shape anisotropy. This energy depends only on the shape of the magnet, and is not an intrinsic property of the material. The shape anisotropy constant for an ellipsoid is

$$K_{shape} = \frac{1}{4}\mu_0 \vec{M}^2(1 - 3\vec{N}) \tag{1.11}$$

where $\vec{N}$ is the demagnetization factor along the easy axis. Other shapes can be approximated to the ellipsoid by multiplying by an efficiency constant.

The second is magnetocrystalline anisotropy. This is an intrinsic property that reflects the crystal symmetry. Magnetization is different when the external field is along different axes. It can be further classified into two types, single-ion anisotropy and two-ion anisotropy. The first is due to the interaction between the electron orbitals and the electrostatic potential created by the rest of the crystal. The electrostatic energy is

lowered when the orbital is along particular direction, and through spin-orbit interaction, the spin moment is aligned preferentially along certain crystallographic direction. The second is due to dipole interaction. For a two-dipole system, the energy is lowered in head-to-tail rather than in side-by-side configuration, so the head-to-tail configuration is favored. The dipole-dipole term vanishes for cubic lattices such as Fe and Ni, but is significant for non-cubic lattices such as hexagonal Co.

For cubic Fe and Ni, the magnetocrystalline anisotropy energy can be written as

$$U_{mcrystalline} = K_1(a_1^2a_2^2 + a_2^2a_3^2 + a_3^2a_1^2) + K_2(a_1^2a_2^2a_3^2) \tag{1.12}$$

where each a is the direction cosine of the magnetization along x, y, z axis. The material we used is permalloy, which is a polycrystalline alloy of Ni and Fe. It has a small anisotropy constant of $150J/m^3$, and is usually omitted.

For hexagonal Co, the magnetocrystalline anisotropy energy can be written as

$$U_{mcrystalline} = K_1 \sin^2\theta + K_2 \sin^4\theta + K_3 \sin^6\theta + K_3 \sin^6\theta \sin 6\psi \tag{1.13}$$

This value for K_1 is $5 \times 10^5 J/m^3$. This whole term, however, is sometimes omitted in micromagnetic simulation for practical purposes.

For magnetocrystalline anisotropy to play a significant role, the structure must be crystalline. In a polycrystalline structure with local crystal grains, the crystalline anisotropy will not favor alignment across the entire structure.

1.3.4 Zeeman Energy

The Zeeman energy accounts for the interaction between the material's magnetization and the external field. It is represented as an integral over the volume of the magnet

$$U_{zeeman} = \frac{-\mu_0}{2} \int \vec{M} \cdot \vec{H}_{external} \, d^3r \tag{1.14}$$

This energy reaches a minimum when the magnetization is parallel with the applied external field.

1.4 Domain Wall Formation

The exchange and Zeeman energies try to align spin magnetic moments parallel to the external field throughout the whole sample, forming a single big domain. However, in order to minimize the demagnetizing field, it is energetically favorable for the big domain to break down into smaller domains. The boundary between neighboring domains is the domain wall (DW).

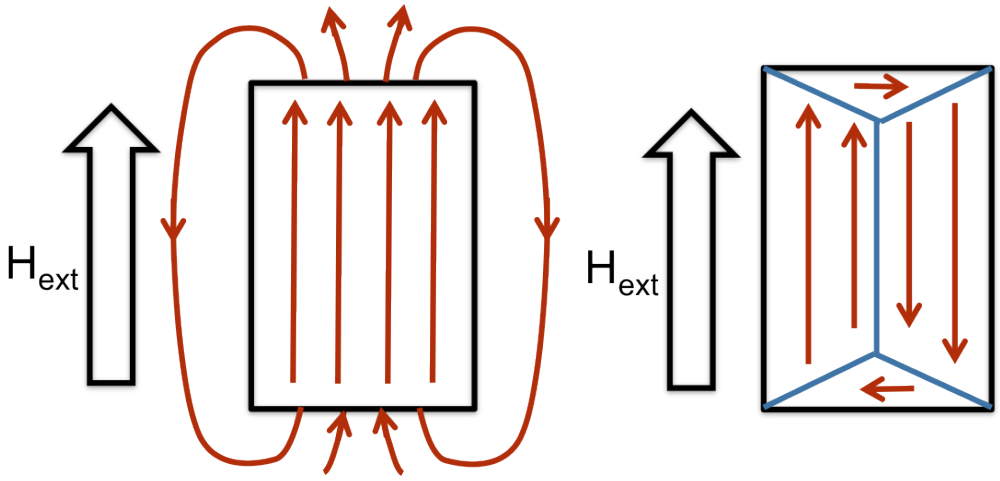

Figure 1.1: Magnetic configuration of ferromagnets without and with domain walls. To minimize the total free energy, magnets break into domains with magnetization pointing in different directions.

Let us examine the formation of magnetic domains (Fig. 1.1). For the magnet on the left, both exchange and Zeeman energies are minimized, as all magnetic moments are parallel to the external field. However, there is a large cost to the demagnetization energy as seen by the large number of field lines outside of the magnet. For the magnet on the right, exchange and Zeeman energies increase in the DW region and in the domains where moments are not parallel to the external field. But the increased energy is outweighed by the large decrease of demagnetization, which is visualized

by the decrease of the stray magnetic field line.

In some structures, we can observe 180° DWs. We call them 180° DWs because magnetic moments are anti-parallel in the neighboring domains, and in the DW region moments rotate 180° degree. We consider two types of 180° domain walls, the Bloch wall and the Neel wall. For a Bloch wall, the magnetic moments rotate within the plane, while for the Neel wall, they rotate perpendicular to the plane. The latter can be observed in thin-film structures where the exchange length is large compared to the structure thickness, so magnetic moments cannot rotate smoothly within the plane. Our structures, albeit thin, is usually 10 nm thick at least and much thicker than the exchange length. However, we may observe Neel walls in experiment due to surface defect. But in computer simulations where everything is ideal, we usually observe Block walls.

The domain wall does not have a precise width. For the Bloch wall, we can define the domain wall width as the distance over which 90% of the rotation has taken place,

$$\delta_{wall} = 4\sqrt{\frac{A}{K}} \tag{1.15}$$

where A is the exchange stiffness related to the exchange parameter J, and K is the anisotropy constant. The domain wall width usually varies from several to a hundred nanometers. The energy per unit domain wall area is

$$\epsilon_{wall} = 4\sqrt{AK} \tag{1.16}$$

In summary, I have introduced background physics of how general energy terms dictate the magnetic configuration of ferromagnetic structures. In chapter 2, I will discuss the motivation for my project on the zigzag nanowire. I will review the present challenge to realize its potential applications, and previous work done by our group. In chapter 3 and 4, I will elaborate on the computational and experimental approach we use to investigate and manipulate magnetic states in zigzag nanowires. In chapter 5, I will report the simulation and measurement results. I will conclude with discussion and future work in chapter 6.

2. Motivation and Previous Work

In chapter 1, I have discussed general energy terms in ferromagnetic structures. In following sections, I will introduce zigzag nanowires as the main focus of our study. I will discuss the motivation for working on zigzag nanowires. I will start with racetrack memory as a potential application of nanowires. Then I will talk about two popular methods nowadays to manipulate magnetic states in nanostructures: passing spin-polarized currents and applying non-uniform magnetic fields. Finally, I will introduce a novel technique developed by our group, which uses circular magnetic fields to control domain walls. I will conclude with an example where we successfully use this technique to switch magnetic states in nanorings.

2.1 Ferromagnetic Nanowires

I have introduced energy terms in ferromagnetic materials in Chapter 1, and in this section I will discuss how these energy contributions allow us to understand the magnetic states of the zigzag nanowire. The magnetization of a ferromagnet depends on not only the present external field, but also on the past field. This type of dependence on the system's history is hysteresis. And the ferromagnet's magnetization is in the remanent state when an external field is applied and then removed. The ferromagnetic zigzag nanowire exhibits unique magnetic states, and is the topic of my thesis.

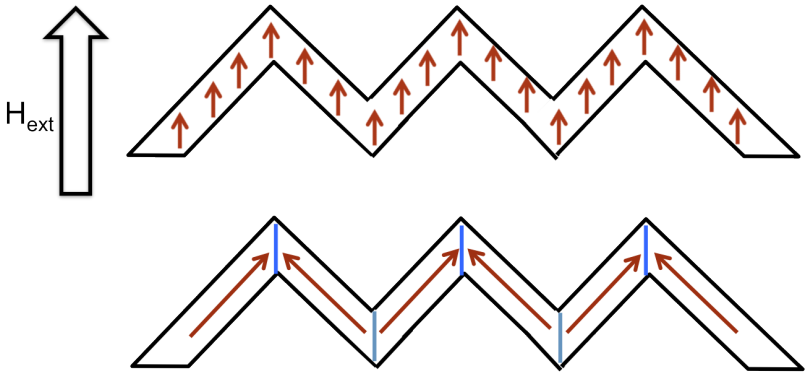

Figure 2.1: Evolution of magnetic configurations of zigzag nanowires in an external field in y-direction. The magnetic moments rotate from pointing upward to pointing along the arms, forming domain walls at vertices.

Depending on the initial direction of the external field, zigzag nanowires have two different remanent states around the zero field. If we start with a strong in-plane field in the y-direction, perpendicular to the the length of wire as shown in Fig. 2.1, the magnetic moments align parallel to the field and perpendicular to the length of the wire. In this state, the Zeeman and exchange energies are minimized at the cost of shape anisotropy energy.

As the external field decreases, the strong shape anisotropy starts to take over at the cost of Zeeman energy. The magnetic moments rotate around the y axis and gradually align with the wire arms. Within each arm, the exchange energy is minimized. The moments along neighboring arms are opposite, forming 180° domain walls in vertices.

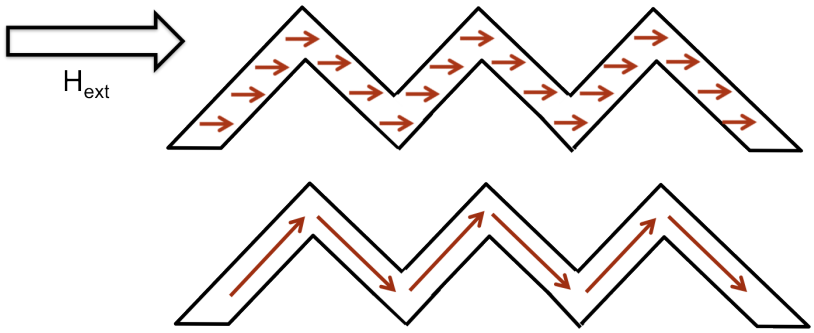

Figure 2.2: Evolution of magnetic configurations of zigzag nanowires in an external field in x-direction. The magnetic moments rotate from pointing toward right to pointing along the arms continuously. There are no domain walls.

If we start with a strong in-plane field in the x direction and parallel to the wire, the magnetic moments align parallel to the wire, as shown in Fig. 2.2. In this state, Zeeman and exchange energies are minimized at a cost to shape anisotropy energy. When the field relaxes, the magnetic moments rotate slightly around the x axis and also gradually align with the arms. This time, the moments along neighboring arms are in the same direction, forming continuous turnings in vertices.

While both parallel and perpendicular states exhibit interesting physics, we mainly investigate the perpendicular case. The perpendicular case forms domain walls in the remanent state, which can be potentially moved around in different ways.

2.2 Racetrack Memory

Magnetic domain walls in wires have great potential applications in storing digital data. A good example is *racetrack memory*, which was first demonstrated by Stuart S. P. Parkin 's group at IBM Almaden Research Center [3]. The main types of digital memories today are solid-state memories and magnetic hard drive disks (HDDs). Solid-state memory is fast, with a typical access time of several nanoseconds to several microseconds. It is also more durable against physical damage than HDD. On the other hand, the cost of HDD is considerably cheaper than solid-state memory, with a cost per gigabyte of several cents. The disadvantage of HDD is its low access time of several milliseconds, due to the nature of a rotating disk and moving read head. The racetrack memory proposal combines the low cost of HDD and the high speed and reliability of solid-state memory. In racetrack memory, data are encoded along the wire with magnetic domain walls. For example, " 1 " corresponds to a head-to-head 180° DW and " 0 " corresponds to a tail-to-tail 180° DW. DWs form at pinning sites along the wires, and head-to-head and tail-to-tail appear alternatively. The pinning sites can be achieved in different geometries. In previous section, the pinning sites are vertices along the zig-zag wire; in Parkin's proposal, they are a series of notches along a straight wire. (Fig. 2.3)

Fig. 2.4 shows the schematic drawing of the proposed 3D racetrack memory device. A series of head-to-head and tail-to-tail DWs are stored in a wire, encoding the data. The DW series passes through reading and writing heads. Reading data is accomplished by the magnetic tunnel junction (MTJ) structures near the wire. MTJ is a layered structure with two ferromagnetic layers separated by an insulating layer. MTJ displays the property of magnetoresistance, meaning that its electric resistance changes

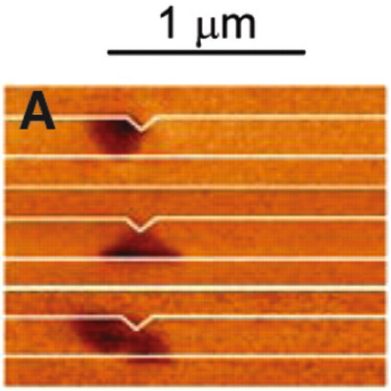

Figure 2.3: Detailed structures of domain walls near one notch of a wire. The wire is delineated with the white line, 10 nm thick and 200 nm wide. There are a series of notches placed at equal distances apart along the wire. This structure is fabricated at IBM Almaden Center in S.P. Parkin's group [3].

depending on the local magnetic field. Head-to-head and tail-to-tail DWs apply opposite fields near the MTJ, thus changing its resistance. Therefore, we can read data by measuring the magnetoresistance of the MTJ structure. Writing data can be accomplished by manipulating the magnetization in a wire nearby the racetrack. We can move a DW in the nearby wire, and the stray field from that DW can change the domain orientation in the racetrack, therefore writing new data in the memory.

Many prototypes of racetrack memories have been proposed. However, it is essential understand more of the fundamental physics of DWs before we can realize the racetrack memory in production. For instance, how fast the DW moves affect the speed of the memory, and how close we can put two domain walls together determines the smallest bit-length in the memory. Therefore, we set out to explore DWs' motion and interaction in zig-zag nanowires.

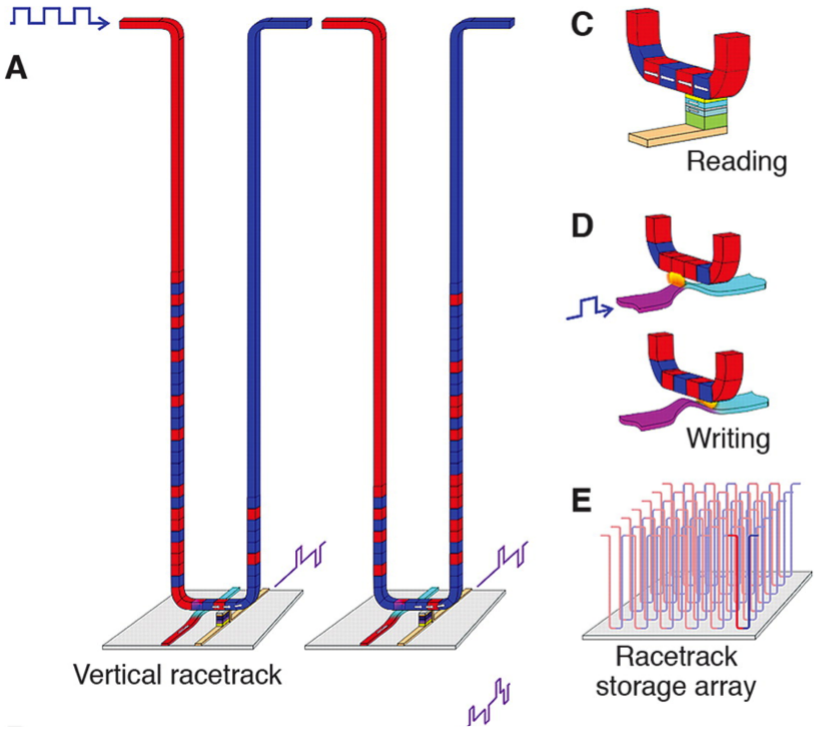

Figure 2.4: (a) and (e) show an individual racetrack and a racetrack array. (c) and (d) show the read head and the write head, respectively [3].

2.3 Present Methods to Control Domain Walls

There are two main methods to move the DWs in a racetrack in a controlled fashion passing spin-polarized current pulses[8, 9, 10] and applying non-uniform magnetic fields [4, 11]. I will explain both in detail in the following paragraphs.

It is possible to move domain walls by passing currents. In Fig. 2.5 , two domain walls indicated by dark and white contrasts are driven to the same direction by current pulses. Between each successive graph, a current pulse of 26 mA and 14ns is applied. The two domain walls move simultaneously from the right to the left. The current and the domain wall

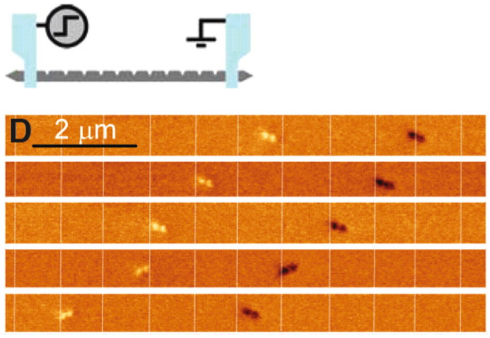

Figure 2.5: Two domain walls move simultaneously from right to left. The cartoon at top shows a schematic of the experiment. Experimental results are shown for a 40-nm-thick, 100-nm-wide permalloy nanowire with 11 triangular notches located 1 μm apart. Single current pulses, 8V (26 mA) and 14 ns long, were applied between each image sequentially from top to bottom [3].

interact through a momentum transfer and a spin transfer. The current transfers momentum to the wall, leading to the wall motion. This momentum transfer between the wall and electrons occurs when the electrons are scattered off the wall. The magnitude of transfer is proportional to charge

current and wall resistance. The spin transfer occurs when electrons pass through the wall and their spin must change as they pass from one magnetized domain to the oppositely magnetized domain, and is proportional to the spin current. As stated in section 1.1, an electron has a spin, pointing either up or down. Usually, a current flow consists of about half of spin-up electrons and half of spin-down electrons. When a current passes through a magnetized material, electrons are polarized in a way that electrons with a certain spin outnumber those with opposite spin. Therefore, a spin current is generated in addition to the charge current. Due to the mismatch between spin in the current in the wall region and those in the domain wall, the spin current exerts a force on the domain wall, rotating the spins in the wall, effectively pushing the wall farther along. The spin-polarized current exerts the same force on both head-to-head and tail-to-tail domain walls.

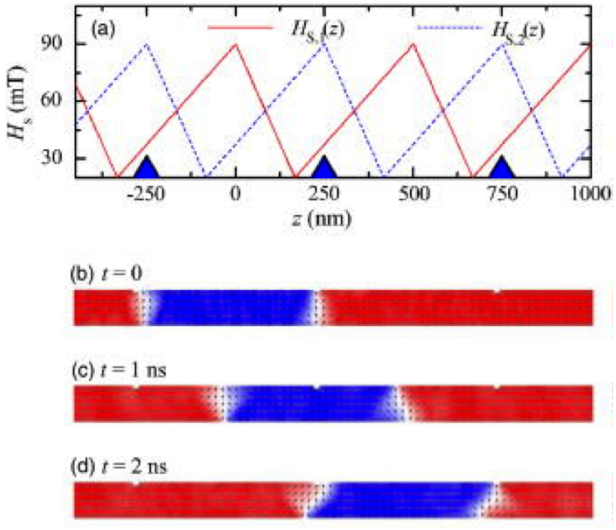

Figure 2.6: Two domain walls move simultaneously from left to right under non-uniform fields. (a) shows the two fields applied between 0 to 1 s and 1 to 2 s, respectively. (b) to (d) show the snapshots of the wire at 0, 1, 2s in the field [4].

It is also possible to move domain walls in a non-uniform magnetic

field. Simulations have shown that a head-to-head and a tail-to-tail domain wall move together to the same direction in a well-designed linear field. (Fig. 2.6)This movement is only possible in non-uniform fields, because domains with opposite orientations react differently in a uniform field. The domain aligning in the same direction with the external field expands, and the domain with the opposite direction shrinks. The head-to-head and tail-to-tail domain walls will move either toward each other or separate further apart in a uniform field. Field-driven method has certain advantages such as no heating. However, field-driven method is less favorable than current-driven method, as it is more complex and expensive to construct a certain non-uniform magnetic field.

2.4 Domain Wall Manipulation in a Local Magnetic Field

Our group developed a novel technique to manipulate magnetic domain walls by applying local circular magnetic fields [1, 2]. We pass current to a conducting AFM tip, hence by Ampere's law a circular magnetic field forms around the tip. The field strength B at a distance r away from the current I is

$$B = \frac{\mu_0 I}{2\pi r} \tag{2.1}$$

We can precisely locate the tip position across the sample, and therefore affect the magnetic state of individual nanostructures. Fig. 2.7 shows the schematic circuit diagram for passing current through AFM tip.

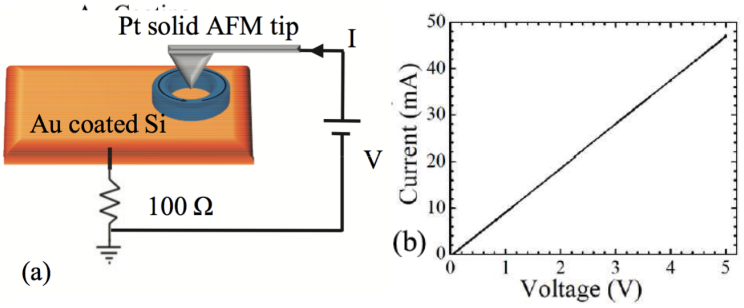

Figure 2.7: (a) Cartoon shows the experimental set-up for passing current through AFM tips. (b)The IV curve corresponds to a 100 Ω resistance in the circuit [2].

Our method allows further study of interactions between individual domain walls. With both methods described in section 2.2, domain walls move uniformly. As the device size shrinks down, the domain wall interaction eventually will become prominent. We would like to explore questions, such as how close two domain walls can be placed together and how hard

it is to separate them apart. Therefore, it is desirable to move individual domain walls in a controlled way.

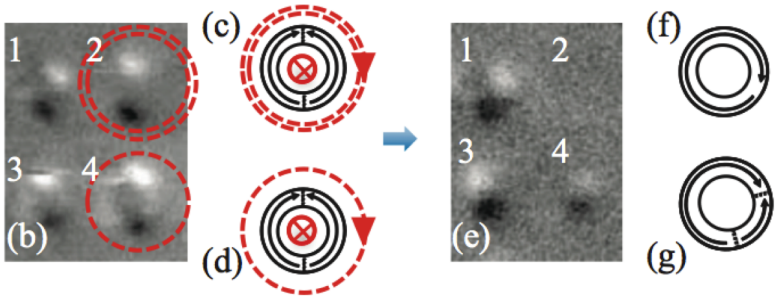

Figure 2.8: Magnetic states of nanorings before and after currents are passed. Rings have outer diameter 1200 nm, inner diameter 900 nm. Ring 2 ends in the vortex state, where both walls annihilate. Ring 4 shows that the walls have moved but not annihilate [2].

We have had previous success in manipulating the magnetic state of nanorings. Fig. 2.8 shows Below are the magnetic force images of four nanorings before and after current is passed through. Originally, the four rings are in the onion state in Fig. 2.8 (b) to (d). In this state, the ring is divided to two domains, clockwise and counter-clockwise. There is a head-to-head domain wall indicated by the dark spot at the top and a tail-to-tail domain wall indicated by the bright spot at the bottom. To the center of the two right rings, we pass current that results in a clockwise magnetic field. The top right 2 in (e) is in the vortex state with a single domain. The anti-clockwise domain aligning against the applied clockwise field switches entirely to the clockwise orientation. There is no domain wall so there is no contrast in the graph. We apply less current to the bottom ring 4 in (e). In this case, the counter-clockwise domain does not diminish completely, and the two domain walls are brought closer. In the graph, the dark and bright spots are close together.

We would like to extend our ability to manipulate domain walls from rings to wires. Our methods using local circular magnetic fields allows greater study on magnetic domain wall interactions which are key to realize racetrack memories. But before I move on to the experimental setup, I will first introduce simulation methods in chapter 3 as it provides valuable guidance to perform experiments.

3. Computational Methods

We study magnetic configuration of nanostructures through computational simulations. These simulations help us to predict novel states and provide qualitative references to guide us in experiments. We perform simulations with Object Oriented Micro Magnetic Framework (OOMMF) [12], which integrates the Landau-Lifshitz-Gilbert (LLG) equation to calculate the magnetic configuration of the sample. In this chapter, I will first discuss the overall procedure to run simulations, and then elaborate on the phenomenological derivation of the LLG equation [13].

3.1 Overview of Simulation Procedure

Evolution of magnetization in nanowires is studied with simulations. The program we use is Object Oriented Micro Magnetic Framework (OOMMF), a public domain program provided by NIST. The main contributors are Mike Donahue and Don Porter. This program uses the LLG equation to calculate the evolution of magnetic moments, and I will elaborate on it in the next section. For a faster computational speed, we run simulations at computer cluster Odyssey at Havard University. I will introduce the general procedure to perform simulations, and please refer to the appendix of Abigail Licht's thesis for a more detailed instruction[14].

OOMMF use *finite element method*, which models a 3D object by breaking it into small pieces containing the material property of the object. Therefore, we need to specify the sample's geometric properties before running simulations. OOMMF then applies a specified magnetic field and uses LLG equation to evolve the equilibrium magnetization at that field. The equilibrium magnetization may differ from the previous magnetization, and OOMMF then takes the new configuration as the initial state, and solves the new equilibrium state of the sample under the next applied field.

To run simulations, we first use MATLAB to generate a 2D mask file to describe the sample's geometry. This file is then transferred to a bmp graphic file. We complete the 3D definition of the sample by specifyng the sample's height and the cell size in a magnetization information file, MIF. We also specify sample's material property, such as exchange energy and crystalline anisotropy in the MIF file. In literature, the exchange energy constant is $1.3 \times 10^{-12} J/m$ and $3 \times 10^{-12} J/m$, and the crystalline anisotropy is $150 J/m^3$ and $5 \times 10^5 J/m^3$ for NiFe and Co, respectively. The crystalline anisotropy for NiFe is small enough to neglect. In real work, we

often set the crystalline anisotropy of Co to be zero for two reasons. First, it is suggested by many other groups that for thin film Co sample, the crystalline anisotropy points randomly and averages to zero for the whole sample. Secondly, a non-zero anisotropy parameter produces noisy results that are hard to interpret, especially in long wire structures, and does not seem to correspond to experimental observations.

When beginning with a new geometry, we start by evolving the magnetization in a series of in-plane uniform field. This helps us to understand the general behavior of the structure and predict the initial magnetization states that we can realistically obtain experimentally. We describe the in-plane field in MIF files. We apply a series of uniform fields with different strengths and find the remanent state at approximately zero field, which is the state that we could experimentally control before applying a circular field. We apply a circular field in MIF file as well. We can calculate the field by locating a current at a certain position. We then put the field strength at the center of the circular field and current location in the MIF file.

As OOMMF evolves the magnetic states, it records many parameters including energy terms in the process. We specify how often to save the magnetic configuration and can visualize the process by looking through these files. This helps to study novel magnetic states, and qualitatively predicts experimental results.

3.2 LLG equation derivation

The LLG equation forms the foundation of OOMMF and calculates the precessional motion of magnetization:

$$\frac{d\vec{M}(\vec{r})}{dt} = -\frac{\gamma_0}{1+a^2\gamma_0^2}[\vec{M}(\vec{r})\times\vec{H}] + \frac{a\gamma_0^2}{(1+a^2\gamma_0^2)|\vec{M}|}\vec{M}(\vec{r})\times[\vec{M}(\vec{r})\times\vec{H}] \quad (3.1)$$

First consider a magnetic moment $\vec{m}$ in an external magnetic field $\vec{B}$. The field exerts a torque on the moment if the moment is not aligned with the field.

$$\vec{\tau} = \vec{m}\times\vec{B} \quad (3.2)$$

This torque is the rate of change in angular momentum $\vec{L}$. It does not change the length of the magnetic moment, but makes the moment precess around the field B at a constant angle.

$$\frac{d\vec{L}}{dt} = \vec{m}\times\vec{B} \quad (3.3)$$

This model applies to spin momentum S as well. Recall equation 1.2, the spin magnetic moment m and spin momentum S is related by :

$$\vec{m} = -\frac{e}{m_e}\vec{S} \quad (3.4)$$

Also, in free space, $\vec{B}$ field and $\vec{H}$ field are related by:

$$\vec{H} = -\frac{\vec{B}}{\mu_0} \quad (3.5)$$

Substitute equation 3.4 and 3.5 back to 3.3, we have

$$\frac{d\vec{m}}{dt} = -\mu_0 \frac{e}{m_e} \vec{m} \times \vec{H} \tag{3.6}$$

This is the precessional motion of a single spin moment in an external field in a vacuum. We can define $\frac{e}{m_e}$ to be γ, the gyromagnetic ratio, which is the ratio between the magnetic moment to its momentum, derived from equation (1.1). And we can write$\mu_0\gamma$ to be γ_0 for further simplicity. Since eventually we are concerned with magnetism in materials, replace single moment $\vec{m}$ with magnetization $\vec{M}$. Therefore we have

$$\frac{d\vec{M}}{dt} = \gamma_0[\vec{M} \times \vec{H}] \tag{3.7}$$

Landau and Lifshitz put this model forward in 1935. According to this equation, the magnetic moment will perpetually revolve around the H field. However, experimental hysteresis curves of ferromagnetic materials show that beyond a saturation field, all moments align parallel to the magnetic field. They propose a damping factor proportional to magnetization M, but it is too small to incorporate experimental fact.

In 1954, Gilbert proposes a damping factor proportional to the time derivative of M, and equation 3.7 is reformulated as:

$$\frac{d\vec{M}}{dt} = -\gamma_0[\vec{M} \times \vec{H}] + a\gamma_0 \frac{1}{|\vec{M}|}[\vec{M} \times \frac{d\vec{M}}{dt}] \tag{3.8}$$

Here a is a dimensionless damping parameter. It is phenomenological because there are many factors involved in determining the damping behavior of moments, and it is too complex to calculate a analytically.

Substitute equation (3.8) for dM/dt in the last term of (3.8), we can

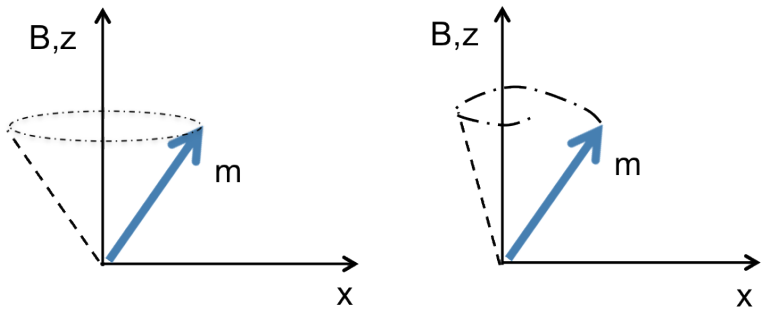

Figure 3.1: A magnetic moment precesses around the magnetic field $\vec{B}$ forever without damping at a constant angle. In reality, the moment eventually aligns to a certain direction.

rewrite equation (3.8) as

$$\begin{aligned}\frac{d\vec{M}}{dt} &= -\gamma_0[\vec{M}\times\vec{H}] + a\gamma_0\frac{1}{|\vec{M}|}\{\vec{M}\times[\vec{M}\times\frac{d\vec{M}}{dt}]\} \\ &= -\gamma_0[\vec{M}\times\vec{H}] - a\gamma_0\frac{1}{|\vec{M}|}\vec{M}\times[\vec{M}\times\vec{H}] \\ &\quad +a^2\gamma_0\frac{1}{|\vec{M}|^2}\vec{M}\times[\vec{M}\times\frac{d\vec{M}}{dt}] \end{aligned} \tag{3.9}$$

The cross product in the last term can be rewritten by Lagrangian equation:

$$\vec{M}\times[\vec{M}\times\frac{d\vec{M}}{dt}] = \vec{M}(\vec{M}\cdot\frac{d\vec{M}}{dt}) - \frac{d\vec{M}}{dt}(\vec{M}\cdot\vec{M}) \tag{3.10}$$

The first term in equation (3.10) is zero because by equation (3.7), $\vec{M}$ and $\frac{d\vec{M}}{dt}$ are perpendicular to each other and therefore have a dot product of zero. So we can rewrite equation (3.10) as:

$$\vec{M}\times[\vec{M}\times\frac{d\vec{M}}{dt}] = -\frac{d\vec{M}}{dt}|\vec{M}|^2 \tag{3.11}$$

Substitute equation (3.11) to (3.9), we get a formula representing the mag-

netization evolution of a discrete, non-interacting spin moment i under an external field $\vec{H}$.

$$\frac{d\vec{M}_i}{dt} = -\frac{\gamma_0}{(1+a^2\gamma_0^2)}[\vec{M}_i \times \vec{H}] + \frac{a\gamma_0^2}{(1+a^2\gamma_0^2)|\vec{M}|}\vec{M}_i \times [\vec{M}_i \times \vec{H}] \qquad (3.12)$$

In a real ferromagnetic sample, an effective $\vec{H}_{eff}$ replaces the external $\vec{H}$ field in 3.11. The applied external field, exchange energy between neighboring spins, demagnetization field, and anisotropy energy described in Chapter 1 all contribute to the effective $\vec{H}$ field.

Until now, we use the local magnetization $\vec{M}_i$ to represent a series of discrete spins, and it varies rapidly on a subnanometer scale. To evaluate this fluctuating system, it is useful to define a mesoscopic $\vec{M}(\vec{r})$ which can be viewed as the average of $vecM_i$ over a small distance, so we can have a continuous magnetization $\vec{M}$ over the sample.

$$\frac{d\vec{M}(\vec{r})}{dt} = -\frac{\gamma_0}{1+a^2\gamma_0^2}[\vec{M}(\vec{r}) \times \vec{H}] + \frac{a\gamma_0^2}{(1+a^2\gamma_0^2)|\vec{M}|}\vec{M}(\vec{r}) \times [\vec{M}(\vec{r}) \times \vec{H}] \quad (3.13)$$

This is the Landau-Lifshitz-Gilbert equation for the magnetization evolution. The OOMMF program calculates the cell-wise integration of the LLG equation to map out the magnetization across the sample.

To sum up, micromagnetic simulations are performed using the OOMMF program that uses LLG equation to evolve the cell wise magnetization of the 3D sample. The LLG equation describes the torque each moment in each cell experiences and predicts the evolution of the moment based on the $\vec{H}_{eff}$ field it experiences. This $\vec{H}_{eff}$ is determined by the fundamental energy terms described in Chapter 1.

4. Experimental Methods

Along with simulations, we study magnetic states of nanowires through various experimental methods. We first fabricate samples with Electron Beam Lithography (EBL). We measure the sample's topography with Atomic Force Microscopy (AFM). We generate a local magnetic circular field by passing current through a conducting AFM tip. With this field, we manipulate magnetic states of nanowires and move magnetic domain walls around. The magnetic configurations are measured with Magnetic Force Microscopy (MFM) before and after applying the circular field. In this chapter, I will explain the methods involved in the experimental processes.

4.1 Sample Fabrication

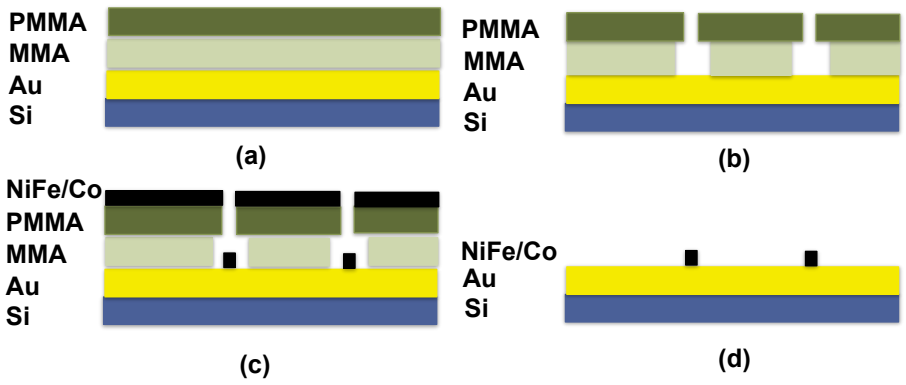

Figure 4.1: The cross-section of the sample through out the fabrication. (a) Spin coating (b) E-beam writing and development(c) Metal deposition (d) Lift-off.

We prepare samples with Electron Beam Lithography (EBL), evaporation, and lift-off in the Conte Nanotechnology Cleanroom Lab at the University of Massachusetts, Amherst. A schematic drawing of the sample preparation is provided in Fig. 4.1. The basic idea is that we deposit some material called "resist on gold and silicon substrate (Fig. 4.1 (a)). We use EBL to write patterns on the resist, and the resist hit by electrons can be washed away, directly exposing the substrate (Fig. 4.1 (b)). We then deposit magnetic material onto the exposed substrate and the remaining resist (Fig. 4.1 (c)). Finally, we lift off the left resist and leaving magnetic structure on the sample (Fig. 4.1 (d)).

We start with a silicon substrate and deposit a layer of gold to allow for electric conduction. The gold layer is deposited with a CHA SE-600 electron beam evaporator, and it is roughly 30 nm for reliable conduction. Fig. 4.2 illustrates the schematic design of a typical ebeam evaporator. In its vacuum chamber, the machine ejects an electron beam from a filament.

It uses the high energy of the electron beam to melt metal, which evaporates and lies on the sample. We can program to control the growth rate and desired thickness.

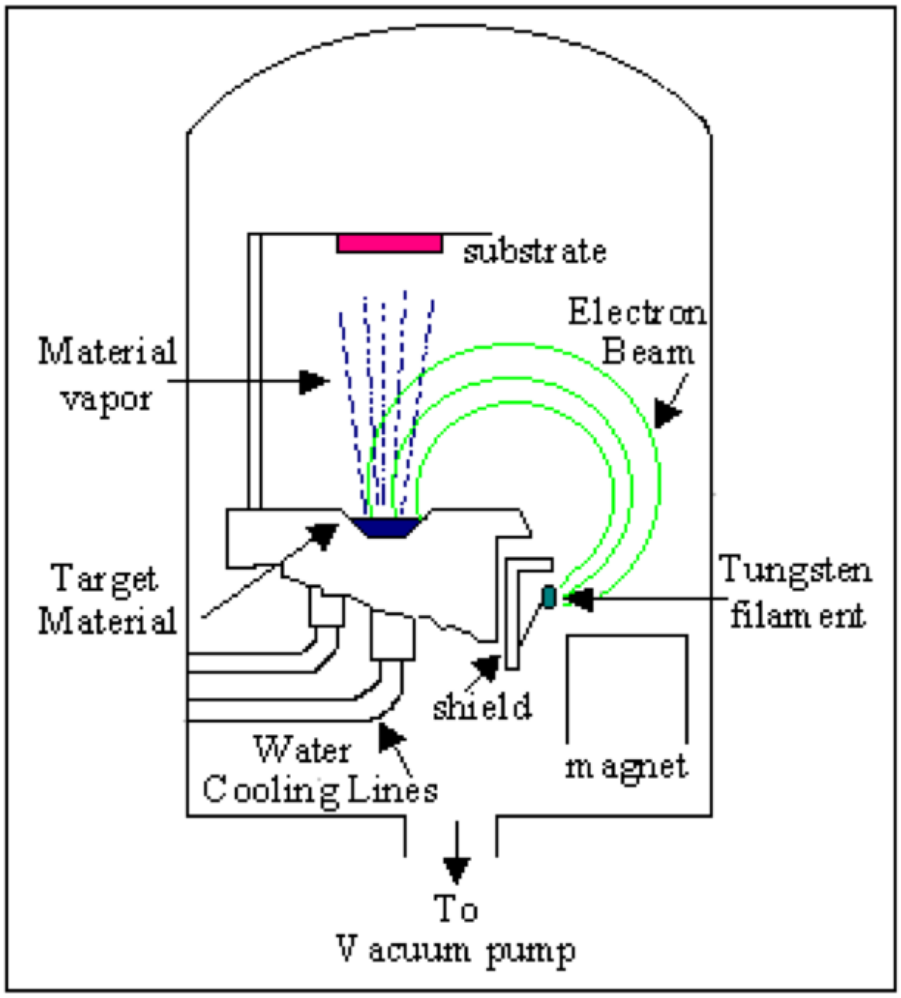

Figure 4.2: Schematic graph showing major component of a typical electron beam evaporator. The electrons are ejected from a tungsten filament. The electrons hit the target material (NiFe/Co) so that the material evaporates onto the substrate due to the heat [5].

We then spin-coat a bi-layer of polymer films as the resist: methyl methacrylate (MMA) on the bottom, and polymethyl methacrylate (PMMA) on the top (Fig. 4.1 (a)). MMA and PMMA consist of long carbon bond chains. Both are positive resists, as they become soluble to photoresist

developer after being exposed to electron beams. They distinguish from negative resists, which become insoluble to developer after being exposed to electron beams. PMMA and MMA respond to electrons, deep UV light as well as x-ray.

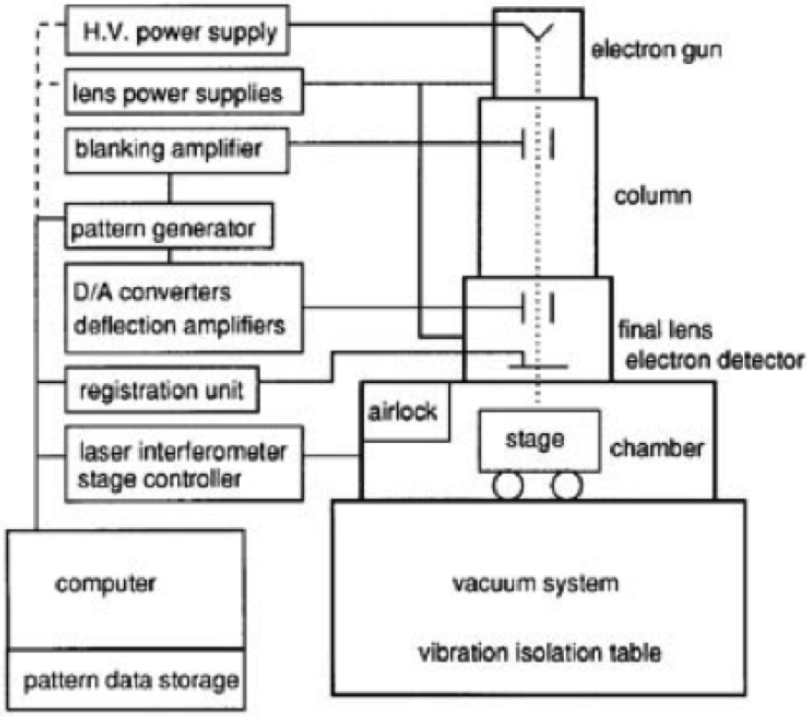

Figure 4.3: Block diagram showing the major component of a typical e-beam writer [6].

We use a JEOL JSM-7001F Ebeam Writer to control the electron beam and write patterns on the resist layer. Fig. 4.3 is the schematic diagram of the machine. We first define the pattern with the AutoCAD program on the computer connected to the Ebeam Writer. Then the electron beam is focused sequentially according to the pattern on the desired location on the sample, therefore writing the structure of our sample. The high-energy electrons are thermally emitted from the electron gun. They hit the sample placed on the stage, and break chemical bonds in the resists.

The electrons mostly responsible for breaking chemical bonds are secondary electrons, which are generated through electrons' inelastic interactions with atoms in the resists. Many factors affect the final resolution of the pattern. To increase resolution, we do many adjustments so that the beam is sharp and perpendicular to the sample stage. That is because if the beam has a large cross-section or is tilted to the sample, the pattern may be too wide or distorted. The Conte Lab has produced samples down to about 20 nm wide. Our thinnest sample is about 180° nm wide. Please refer to Tianyu Yang's thesis section 3.2 for detailed procedures of EBL.

Next, we wash away the PMMA and MMA that are exposed to electron beams with the developer solution and this leaves some gaps in the photoresist layers and exposes the gold layer (Fig. 4.1(b)). Note that PMMA has stronger bonds than MMA and is harder to be altered by ebeam. Therefore, less volume of PMMA is damaged and we have smaller gaps in the top PMMA layer and wider gaps in the lower MMA layer. This is essential to produce clean samples, as explained in next paragraph.

We use the ebeam evaporator to deposit magnetic material, either NiFe or Co, across the whole sample, as shown in Fig. 4.1(c). The material lies either directly on the PMMA layer where we do not want the material to stay or on the gold layer where wires will exist. The small gaps of PMMA layer helps to make clean samples: material coming through small PMMA gaps would not stick on the wide sidewalls of MMA layer. Therefore, samples would have well defined sides after resists are removed.

We have achieved samples as thin as 6 nm, but we usually make them 12 to 15 nm for better MFM signal. To grow thin, even and defect-free samples, we need slow growing speeds, and a low level of vacuum in the evaporator chamber. For an extremely even sample, it is recommended to evacuate the chamber overnight until the pressure reaches $10^{-7}Torr$ range.

In our case, it suffices to evacuate for 30 min and lower the pressure to $10^{-6}Torr$ range. The growth of magnetic material is almost by monolayer, as the growing rate is roughly 1 Angstrom per second.

After the deposition, we remove the resist and the magnetic material adhering on top of polymers, as shown in Fig. 4.1 (d). This is the lift-off process. Only the material lying directly on the gold layer stays, creating our desired pattern. We use acetone to remove the resist, and we usually soak the sample in acetone overnight. Our last step is to deposit a layer of platinum over the entire sample to protect it from oxidization. This is also done with the ebeam evaporator. Samples can stay away from being oxidized up to two weeks in a vacuum box.

This is a general walk-through to fabricate nanowires. It is important to minimize surface roughness as they create extra pinning sites and change the magnetic states of the samples. It is also important to make the sample remove all polymers as the residual polymer blocks current from passing through.

4.2 Atomic Force Microscopy

We use an Asylum Research MFP-3D atomic force microscope (AFM) to visualize topography details of nanowires. AFM is capable of a resolution of a fraction of a nanometer, beating optical microscope's diffraction limit of 200 nm. AFM was invented by G. Binnig, C.F. Quate and C. Gerber in 1985. Fig. 4.4 is a cartoon of a typical AFM machine.

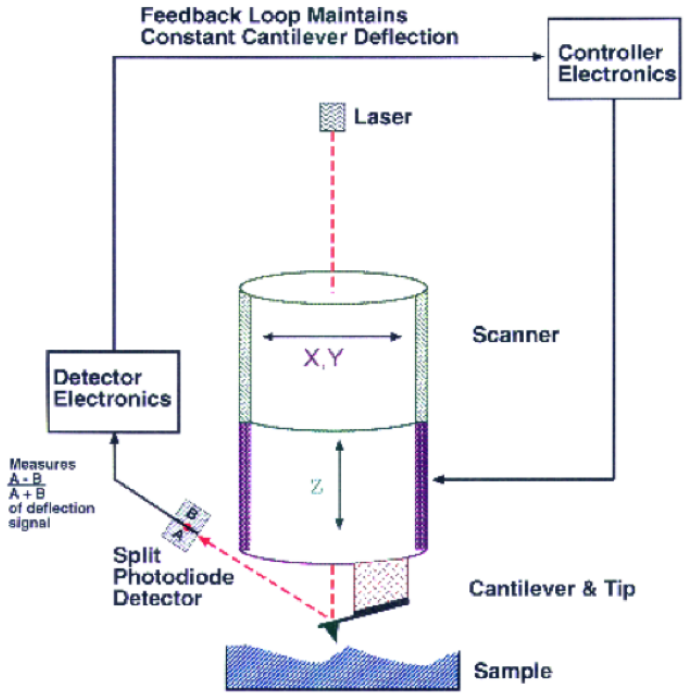

Figure 4.4: Major component of an AFM machine [7].

In AFM, a submicron cantilever tip with a probe sticking vertically down at its head is brought close to the sample surface. The tip deflects due to forces between the sample and the tip. The tip's deflection is measured by reflecting a laser spot on the top surface of the cantilever into a series of photodiodes. As the tip raster scans across the sample surface, the deflection of the tip changes with the force it experiences from the sample. Coupled with the feedback mechanism, a piezoelectric actuator moves the

tip up and down to maintain a constant force between tip and the sample. For instance, the tip moves up when the sample surface rises and the tip moves down when the sample surface lowers. The vertical stage motion is plotted versus planar stage position and therefore a 3D topography image of the sample is obtained.

In AFM topography imaging, we mainly detect Van de Waals force. Van de Waals force is the force between atoms, molecules and surfaces with permanent or induced dipoles. This force is different from electric interactions between ions or the forces due to covalent bonds. We often use the Lennard-Jones potential to approximate the Van de Waals force verses distance between two atoms

$$E_r = -\frac{a}{r^6} + \frac{b}{r^{12}} \tag{4.1}$$

where a,b are parameters known to be $10^{-77} Jm^6$ and $10^{-134} Jm^12$ respectively, and r is the distance between the two atoms. The interaction force, which is the distance derivative of potential energy, is

$$E_r = -\frac{6a}{r^7} + \frac{12b}{r^{13}} \tag{4.2}$$

which is first repulsive and then weakly attractive as r increases. The forces between AFM tip and surface are much larger than the two-body system and the force range is much longer. The force in-between is repulsive.

We usually operate in two modes: contact mode and AC mode. We use AC mode to obtain the topography image of the sample because contact mode risks destroying the sample surface. In contact mode, the cantilever is kept at a constant deflection and is “dragged” across the sample. In

AC mode, the cantilever is externally oscillated slightly below its resonant frequency. The resonant frequency of a typical Si tip that we use is around 80 kHz. The tip is kept at a constant oscillation and barely touches the sample. When the sample surface rises, the repulsive force increases and the oscillation amplitude decreases. Therefore, the stage moves up to reduce the force and maintain oscillation amplitude. Vice versa, when the sample surface lowers, the repulsive force decreases and the oscillation amplitude decreases. Therefore, the stage moves down to increase the force and maintain the oscillation amplitude.

4.3 Magnetic Force Microscopy

We use magnetic force microscopy (MFM) to image the magnetic configuration of nanowires. In MFM, we operate in AC mode and the tip oscillates. During MFM scan, the tip scans along a line twice. First, it performs a regular AFM scan near the sample surface to determine the topography. Secondly, the tip rises up to a constant height above the surface, usually around 40 to 60 nm. At this height, the tip reacts to the force from sample's magnetic stray field rather than the weak Van de Waals force between the sample and the tip.

We measure magnetic configuration of the sample by detecting and plotting a phase image across the sample surface. When the tip is externally oscillated off its resonant frequency as in AC mode, there is a phase shift between the applied force and the tip deflection. Phase is a sensitive indicator of the magnetic force gradient, and from the phase image we can visualize the stray field of the sample. The phase image consists of white and dark contrasts. A white spot indicates a repulsive force between sample and the tip and a dark spot indicates an attractive force. For our current magnetization of the cantilever tip, a white spot corresponds to an out-of-the-plane stray field from the sample and a dark spot corresponds to an into-the-plane stray field from the sample.

The resonant frequency of a cantilever with mass m and spring constant k is

$$\omega_0 = \sqrt{\frac{k}{m}} \tag{4.3}$$

When a small force with frequency ω and amplitudeF_0 is applied to the cantilever, the motion of the cantilever can be described in the following

equation:

$$\frac{\partial^2 d}{\partial t^2} + \frac{\omega_0}{Q}\frac{\partial d}{\partial t} + \omega_0^2(d - d_0) = \frac{F_0}{m}\cos(\omega t) \tag{4.4}$$

where Q is a factor incorporates the intrinsic properties of the cantilever with the damping effect from the ambience, d_0 is the equilibrium distance of the tip to the sample, and d is the tip's instant distance to the surface. On the right side of the equation, it includes the current movement of the tip, the damping effect and the force the spring force the tip experiences as it deflects. The left hand side is the sinusoidal driven force.

This equation leads to the steady-state solution of the tip's distance to the surface

$$d(t) = d_0 + \delta(\omega t + \alpha) \tag{4.5}$$

where δ is cantilever's oscillation amplitude, ω is the actual frequency and α is the phase shift between oscillation and driven force. The phase shift is calculated as

$$\alpha = \arctan\frac{\omega\omega_0}{\omega^2 - \omega_0^2} \tag{4.6}$$

When the cantilever is brought close to the surface, an additional force due to dynamic magnetic interactions between tip and the sample comes to influence the tip oscillation as well. This force F_m effectively changes the spring constant of the cantilever

$$k_{eff} = k - \frac{\partial F_m}{\partial z} \tag{4.7}$$

An attractive with a positive $\partial F_m/\partial z$ decreases the spring constant, effectively softening the cantilever. An attractive with a negative $\partial F_m/\partial z$ increases the spring constant, effectively stiffening the cantilever.

According to equation (4.3), the effective resonant frequency of the

cantilever changes to

$$\omega_{0eff} = \omega_0 \sqrt{1 - \frac{1}{k}\frac{\partial F_m}{\partial z}} \tag{4.8}$$

Provided that $\partial F_m/\partial z$ is much smaller than k, the effective resonant frequency can be rewritten as

$$\omega_{0eff} = \omega_0 (1 - \frac{1}{2k}\frac{\partial F_m}{\partial z}) \tag{4.9}$$

According to equation (4.6), a change in resonant frequency will result in change in the phase shift between oscillation and driving force. The phase shift is experimentally measurable, and is used to map the vertical force gradient $\partial F_m/\partial z$. From the force gradient we infer the stray field from the sample and map the magnetic configuration. In experiments, we have employed high-coercivity tips as they have a stable magnetization and do not switch easily due to the applied in-plane field. We have also used low-moment tips as they are less sensitive to signal noise. High-moment tips are less favored as they switch with the external field easily and produce unreliable results. Also, it is easier to interpret MFM image when there are well-defined DWs as they give strong contrasts in the plot. When complex structures are imaged, simulations can help to understand the underlying configuration.

4.4 Variable Field Module

We use the Asylum Research variable field module (VFM) to apply uniform in-plane magnetic fields in MFM experiments. It incorporates a rare-earth magnet to produce the uniform magnetic field without heating. The maximum field is 2500 Gauss, which exceeds what we need to saturate the nanowire. We can use the VFM to analyze the hysteresis behavior of the nanowires and control the initial state of the wire before applying circular magnetic fields. Slight offset between readings from the built-in software and from a gaussmeter is observed, but the VFM is by and large reliable.

4.5 Creating a Local Circular Field

As introduced in section 2.6, we aim to change the magnetic state of samples with a local circular magnetic field generated by passing current through a conductive AFM tip. Fig 4.5 shows the circuit diagram to pass current and a sample current-voltage curve. I will outline the general procedure here and please refer to the appendix for the step-by-step instruction. We use a

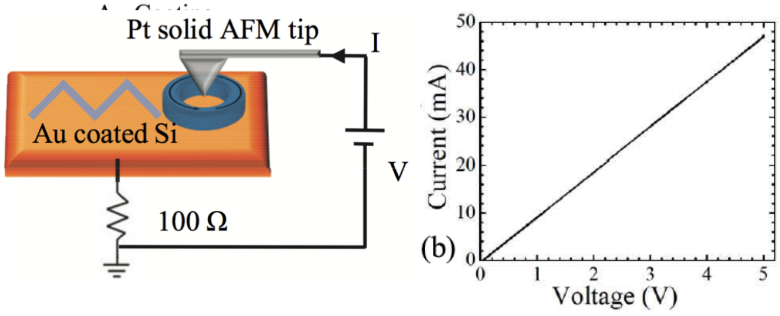

Figure 4.5: (a) Cartoon shows the experimental set-up for passing current through AFM tips. (b)The IV curve corresponds to a 100 Ohm resistance in the circuit.

solid platinum tip which will not easily melt by passing current. We first do a scan in AC mode to obtain sample's topography image and therefore decide where to pass current. We then switch to the contact mode and bring the tip to contact with the surface at desired locations. Note that we do not do a continuous scan in the contact mode, otherwise the sample will be destroyed. We apply a voltage and a current flows from tip to the gold substrate, and through a 40 Ohm resistor to ground. We have repeatedly passed current up to 120 mA, which corresponds to a current density of $5 \times 10^{13} A/m^2$. So far, we have not observed any melting of the tip or the sample due to the large current and its concomitant Joule heat.

In summary, we use various experimental methods to investigate the magnetic configurations of our samples. We fabricate nanostructures with EBL. With AFM and MFM, we measure the topography image, and detect and manipulate the magnetic states of our samples. In the next chapter, I will report the simulation and experimental results of our study on nanowires.

5. Results

In this chapter, I will discuss the simulation and experimental results performed using methods introduced before. In search of the suitable structure to manipulate domain walls, I investigate different structures including zigzag nanowire, curved nanowire and notched nanowires (Fig. 5.1). Curved nanowires are variations of zigzag wires with a series of semi-ellipses instead of triangular corners, and notched nanowires are straight wires with a series of triangular notches like those fabricated by Stuart Parkin's group at IBM. For each structure, I will introduce simulation and experiment results, respectively. In chapter 7, I will discuss these results in greater depth and highlight some future work.

5.1 Zigzag Nanowires

Simulations show that it is possible to manipulate domain walls in zigzag nanowires. By applying local fields, we can move, combine and annihilate individual domain walls. I will introduce how we achieve these manipulations in simulations, and I will continue on showing our experimental progress.

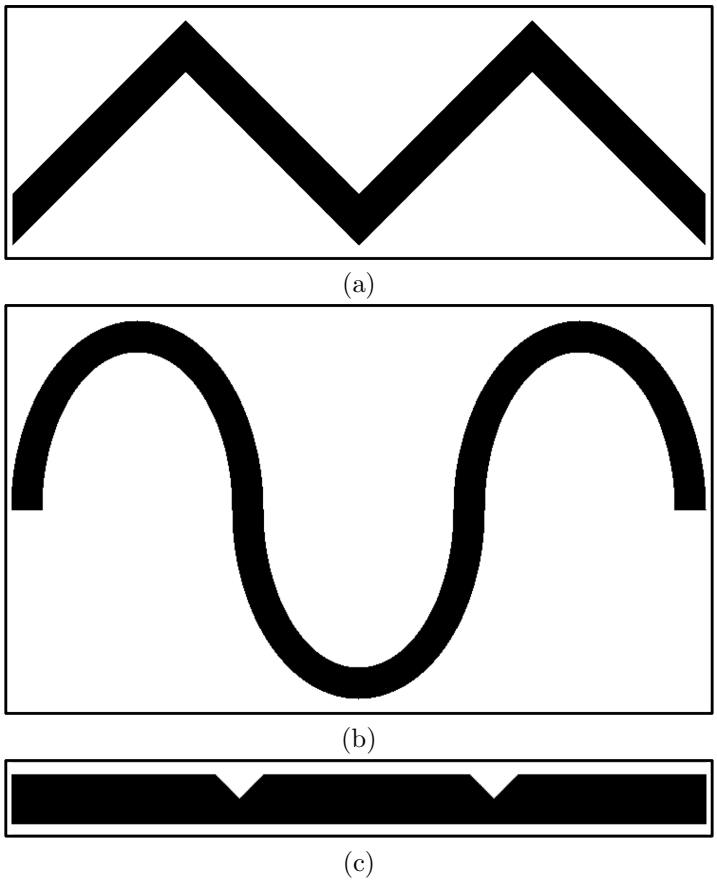

Figure 5.1: (a)A typical zigzag nanowire. (b) A typical curved nanowire. (c) A typical notched nanowire.

5.1.1 Simulation

I initialize the zigzag nanowires to the remanent state with 180° domain walls. From this state, I use a local circular field to move a domain wall toward another domain wall, and these two walls eventually combine. The arm width varies from 100 to 500 nm, and the arm length is 2000 nm. The height is 10 nm.

I get the initial state by applying a field of 4000 Gauss in the y direction and then gradually relax to the 0 field. Originally all moments point up in y direction (Fig. 5.2 (a)). As field decreases, moments rotate and break into domains in each arm. At the remanent state, domains in nearby arms point toward each other, forming 180° domain walls at vertices (Fig. 5.2 (b)). The top walls are head-to-head walls, indicated by red bars, and the bottom wall is a tail-to-tail wall, indicated by a blue bar.

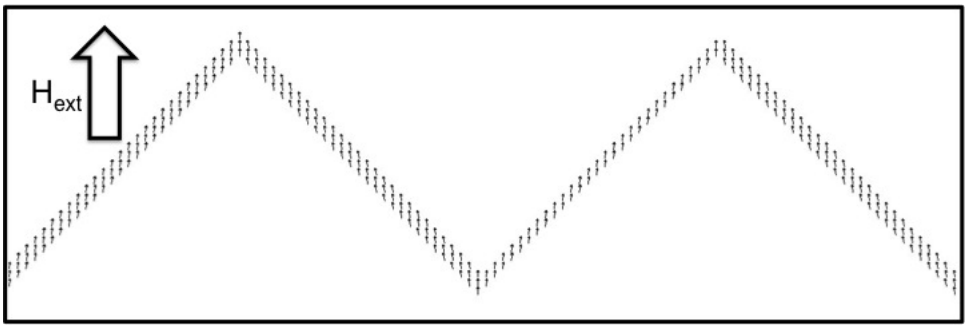

(a)

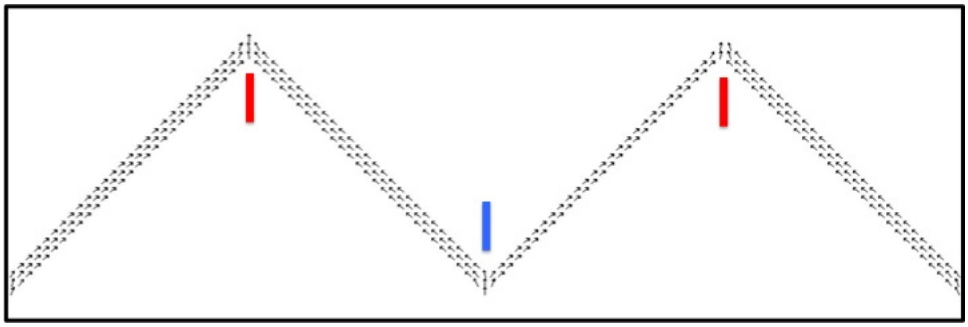

(b)

Figure 5.2: (a) All magnetic moments point up, aligning with the external field. (b) Magnetic moments rotate to align with wire arms as external field decreases.

I then apply a current of 25 mA near the middle vertex. This current goes into the plane and forms a clockwise circular field that is about 33 mT. Moments on the left arm of the current are in the same direction of the field, while the moments on the right arm of the current are in the opposite direction of the field (Fig. 5.3 (a)). Therefore, moments on the right side start to rotate to align with the applied field. This effectively pushes the tail-to-tail domain wall which moves away from the middle toward the top right corner (Fig. 5.3(b) and (c)). Finally, it meets with the head-to-head DW, and they form a 360° DW together. A DW is 360° when all moments in the wall region rotate continuously to form a loop and the moments on both sides of the DW point in the same direction. This 360° DW is stable in a zero field (Fig. 5.3(d)). The 25 mA I passed is the minimum field needed to realize the above movement.

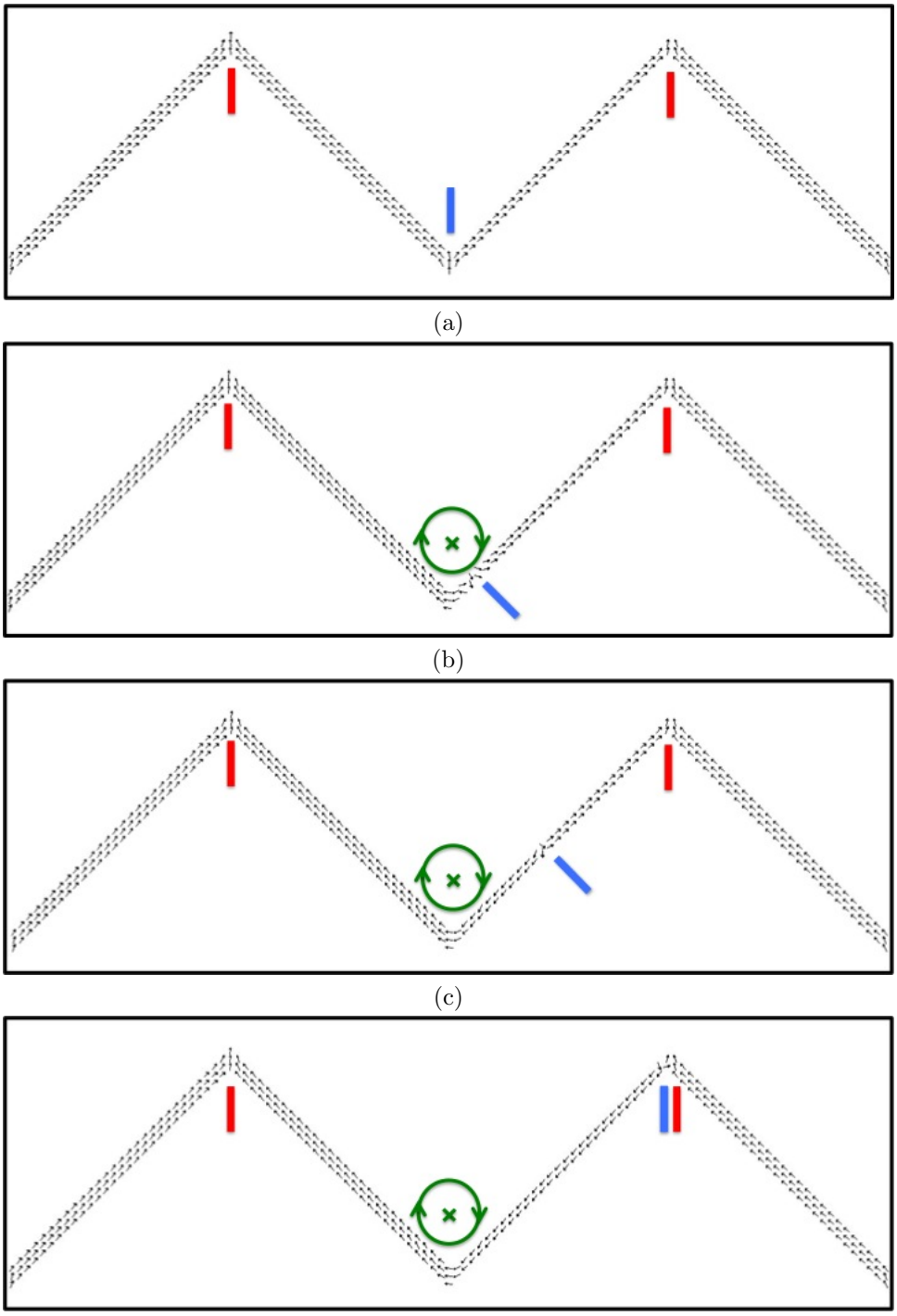

Figure 5.3: (a) The initial state with 180° DWs at vertices. (b) and (c) The 180° head-to-head DW that starts at the middle vertex moves along the arm toward the top right vertex.(d) Two 180° DWs form a 360° DW in the top right vertex.

I can reverse the process and separate the 360° DW. This time I pass a current of 40 mA near the top right corner (Fig. 5.4(a)). This current goes into the plane and forms a clockwise field that is about 53 mT. Moments on both the left and right arms are against the applied field, so all moments start to rotate to align with the applied field. This process effectively separatea the 360° DW into two 180° DWs (Fig. 5.4(b)). The tail-to-tail DW moves down toward the middle corner and stays there. The head-to-head DW moves toward the right end and diminishes there (Fig. 5.4(c)). Indeed, in the picture the head-to-head DW does not go all the way back to the middle corner. But I think it is due to artifact of simulation in the 100 nm wide wire, as both 300 nm and 500 nm wide wires show that the head-to-head DW goes back to its original position (Fig. 5.4(d) and (e)).

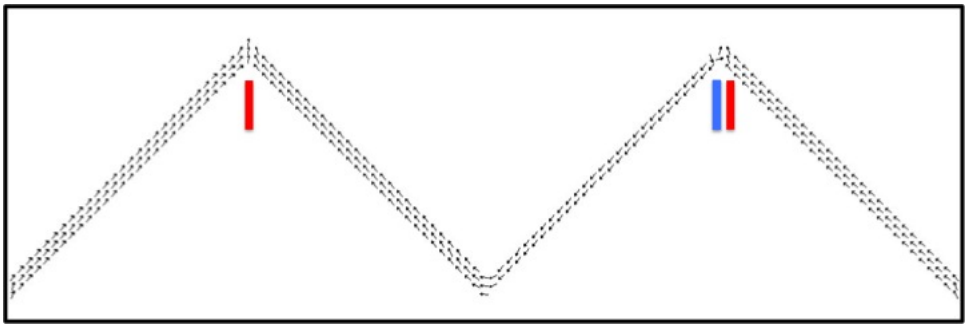

(a)

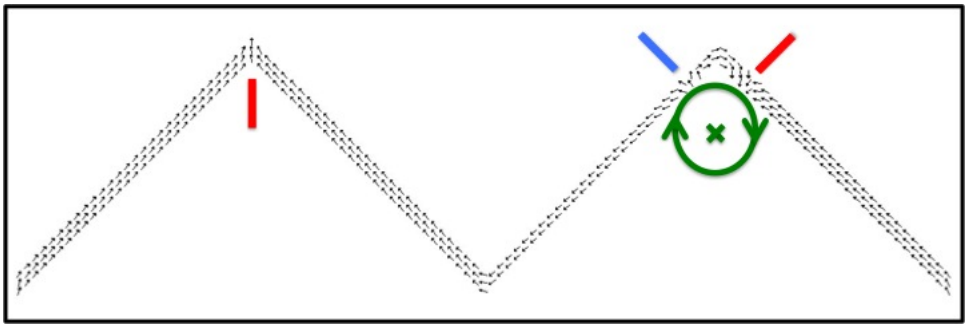

(b)

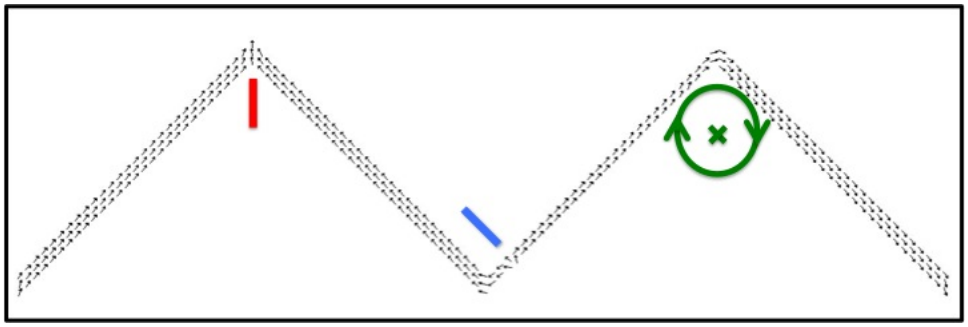

(c)

Figure 5.4

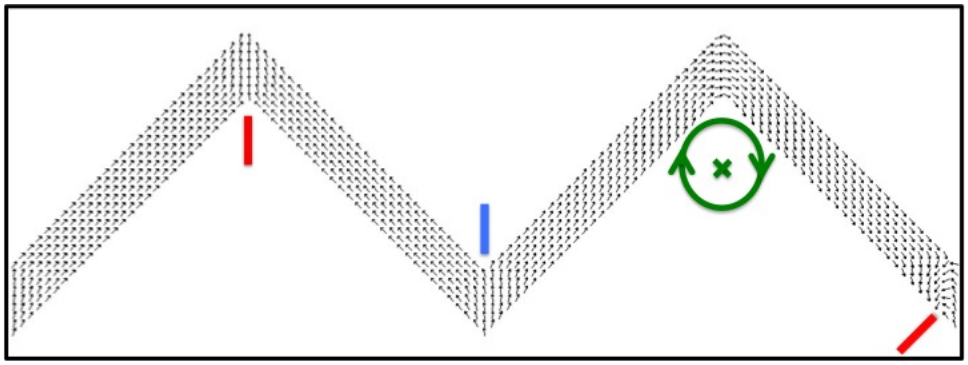

(d)

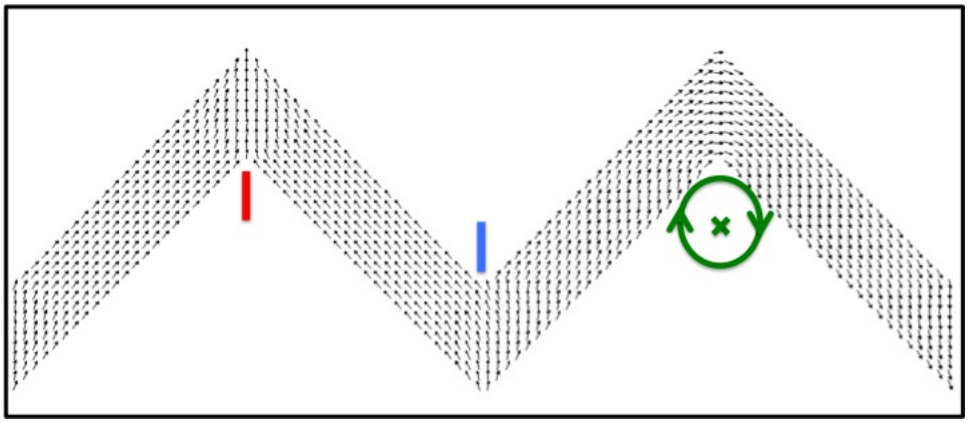

(e)

Figure 5.4: (a)The 360° DW rests in the top right vertex and no DW stays in the middle vertex. (b) The 360° DW separates into two 180° DWs, with one moving along the left arm of the top right vertex and another moving along the right arm of that vertex. (c) The 180° head-to-head DW moves back close to the middle vertex and the tail-to-tail DW diminishes at the right end. (d) For the 300 nm wide wire, the head-to-head DW moves back to rest in the middle vertex while the tail-to-tail DW is pinned at the right end; (e) For 500 nm wide wire, the head-to-head DW moves back to the middle vertex while the tail-to-tail DW diminishes at the right end.

In addition to separating the 360° DW, I can also annihilate it. I pass a current of 40 mA, but out of plane which forms a counter-clockwise field (Fig. 5.5(a)). Moments in the arms around the field are now in the same direction with the applied field, so moments in the wall also rotate to align with the field. This process effectively annihilates the DW wall. Finally, we have no DWs in the middle or the top right corner (Fig. 5.5(b)).

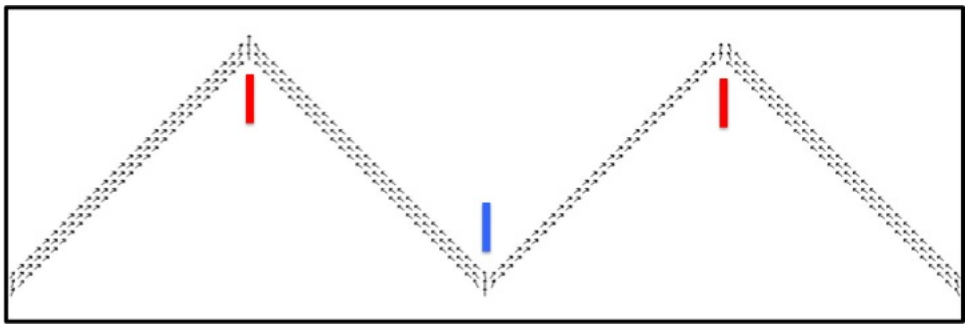

(a)

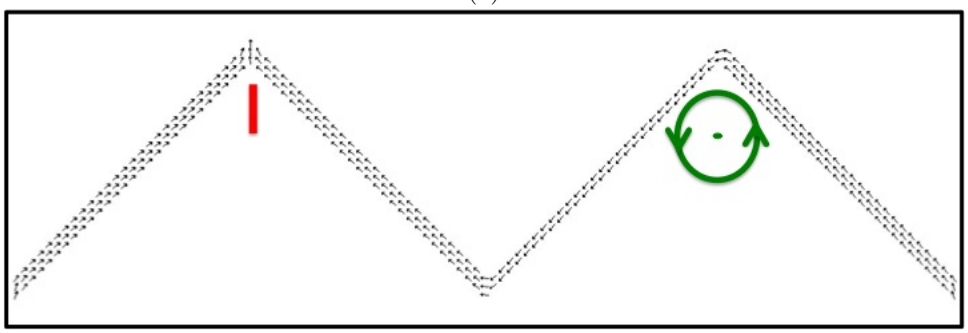

(b)

Figure 5.5: (a) The initial state with 360° DW at the top right corner. (b) The 360° DW annihilates, and there is no DW in the middle or the top right vertex.

To summarize, we can manipulate 180° and 360° DWs in wires with widths from 100 nm to 500 nm. We mainly apply fields around the wire vertices. We have attempted other approaches. For instance, we initialized the wire with the field along the x-direction and applied current onto the wire instead of near the wire. We injected 360° DWs directly at the middle of the arm and in the vertex(Fig. 5.6). These DWs are unstable in a zero field. Although DWs are usually stable in thin structures, these DWs disappear when the sample height is only 5 nm. I do not continue to reduce the height as it is hard to fabricate or image samples that are thinner than that in experiments.

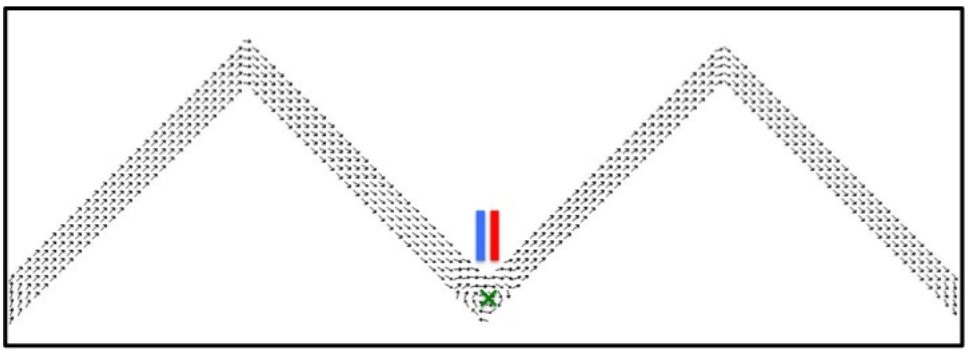

(a)

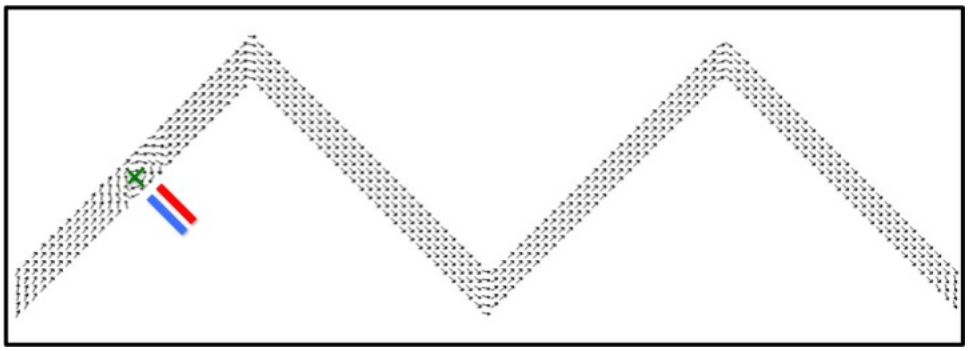

(b)

Figure 5.6: Wires are initialized in the x-direction and there are no DWs in the vertices. 360° DWs are injected (a) in the vertex or (b) in the middle of the arm by with local circular fields.

5.1.2 Experiment

Zigzag nanowires are fabricated with both Co and NiFe. Fig. 5.7 shows a typical topography image of a zigzag wire. The arm width is 236 nm and the height is around 16 nm.

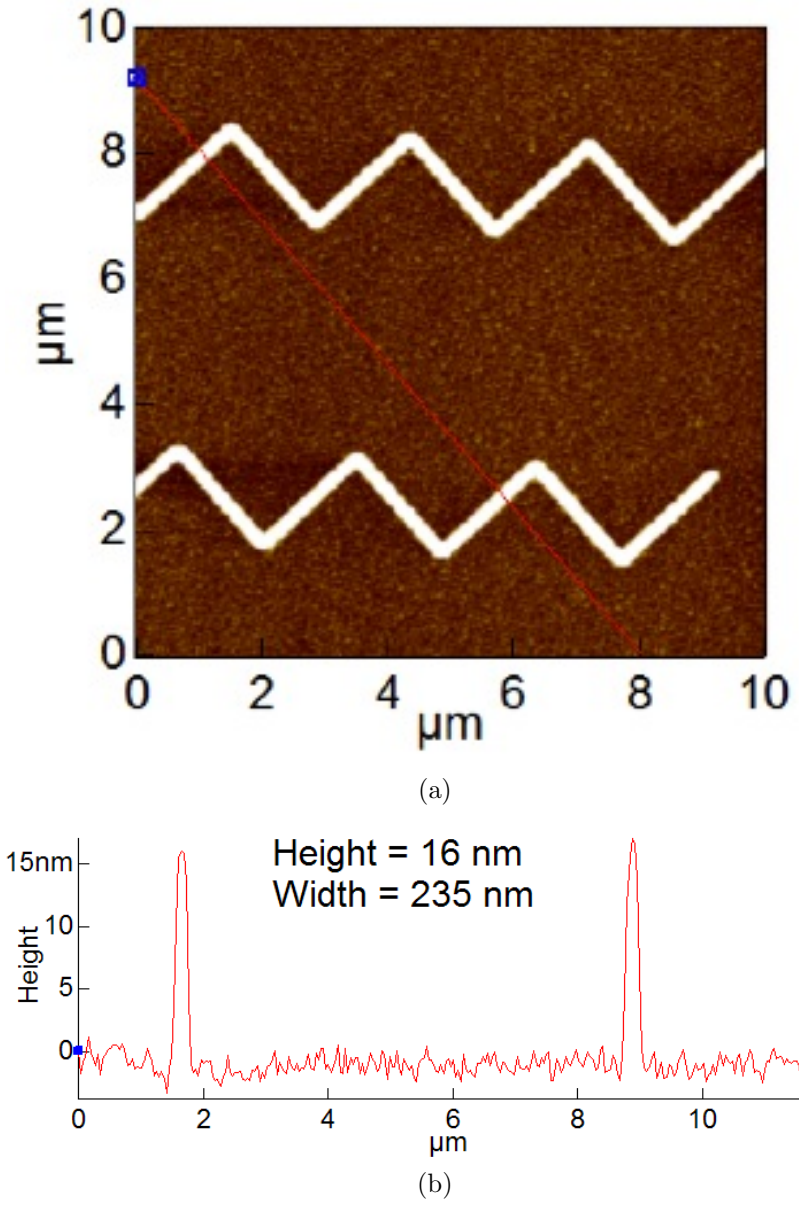

Figure 5.7: (a) top-down topography image of zigzag nanowires; (b) cross-sectional height profile of the sample along the red line in (a).

We obtain MFM images at magnetic fields from -2500 Gauss to 2500 Gauss to observe the general behavior of the wire and to determine the appropriate state to pass current (Fig. 5.8). The MFM images match with simulations well. At high fields, we can see that there is a bright and a dark line on the top and the bottom of the wire, indicating that all moments are pointing in the same direction with the applied field. Near the zero field, the bright and dark lines disappear, and instead we can see dark and bright spots at the vertices, indicating the 180° DWs.

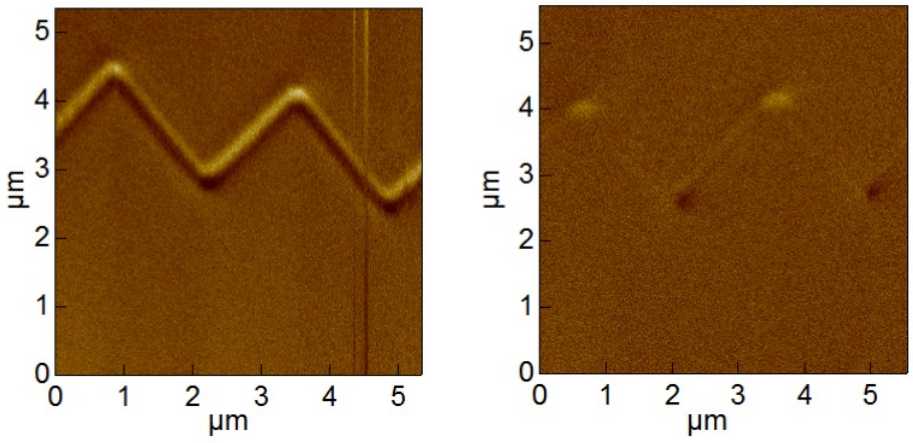

(a) (b)

Figure 5.8: (a) with a strong field in the y-direction, all moments point to the y-direction, forming a bright line on the top and a dark line on the bottom of the wire; (b) at the 0 field, moments point along the arms, forming bright and dark contrasts at the vertices.

Currents have been passed near both head-to-head and tail-to-tail DWs (Fig. 5.9). So far, we have not moved domain walls pinned at the corners, even with a maximum current around 120 mA.

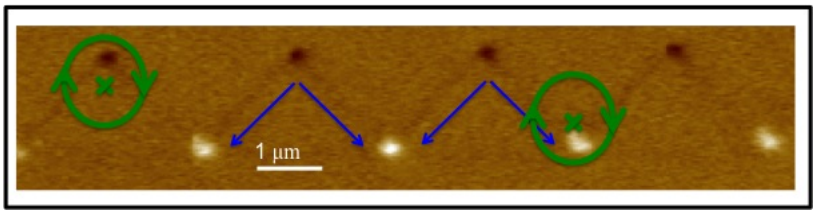

Figure 5.9: We typically pass currents near the head-do-head and tail-to-tail DWs of zigzag nanowires.

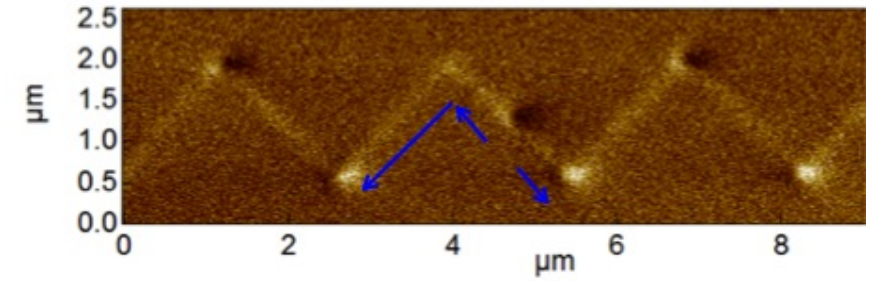

(a)

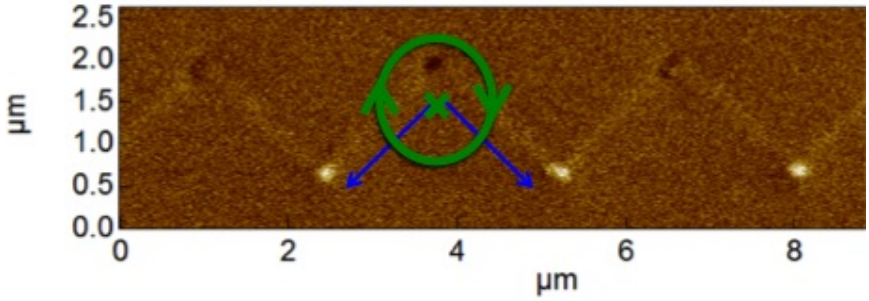

(b)

Figure 5.10: (a) a tail-to-tail DW is naturally pinned at the middle of the arm; (b) this DW moves to the vertex with a clockwise field of 80 mA.

However, one time we have moved a DW pinned at the middle of the arm, probably due to defects (Fig. 5.10). With a current of 80 mA, the DW moves toward the corner and stays there.

In contrast to simulations, we have not yet experimentally accomplished DW manipulations in zigzag nanowires. Simulations predict DW motion at 25 mA, but experiments show no DW motion at 120 mA. This discrepancy is understandable as experiments differ from simulations in many ways. In simulations, structures are homogeneous and free of defects, while in experiments, many defects function as pinning sites to inhibit DW motion. Therefore, simulations lay the blueprint for experiments, but we do not expect quantitative agreements between the applied currents in experiments and those in simulations.

5.2 Curved Nanowires

We modify zigzag nanowires into curved nanowires for two reasons. First of all, the pinning site in curved structures should be weaker than that in zigzag nanowires. In zigzag nanowires, magnetism naturally breaks down into domains along each arm, therefore forming strong pinning sites at the vertices. But the curved wires are roughly homogeneous. Secondly, we have experimentally changed magnetic states in ring structures, so we are making curved wires to resemble a series of semi-rings.

5.2.1 Simulation

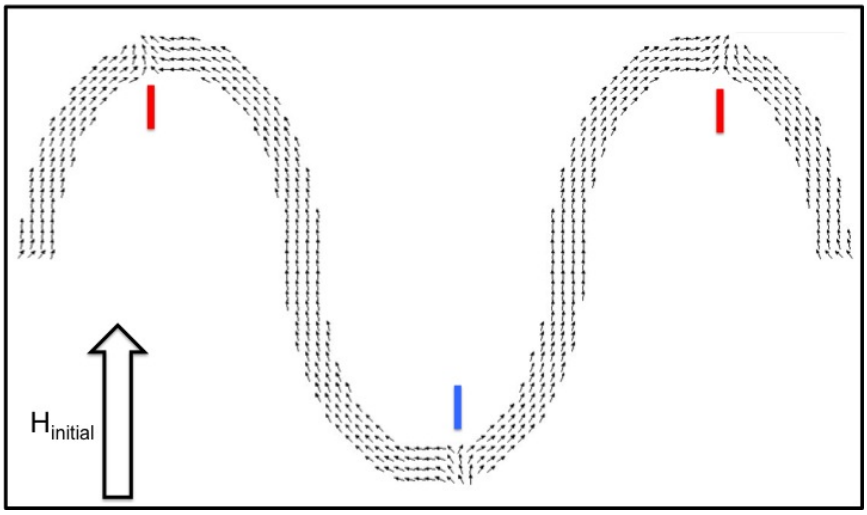

Figure 5.11: Magnetization of a curved nanowire after a strong field in the y-direction is applied and removed.

I initialize the curved nanowire using the same method for zigzag nanowires. The nanowire has a major axis of 1000 nm, minor axis of 600 nm, width of 100 nm and height of 10 nm. The curved nanowire also forms head-to-head and tail-to-tail DWs alternatively at the top and at the bottom of the wires. However, these walls seem less stable. Instead

of sitting right at the vertical symmetry line of each ellipse, DWs start to deflect a little (Fig. 5.11).

When a current is passed, curved nanowires differ greatly from zigzag nanowires as multiple DWs move together. As with zigzag wires, I apply 25 mA of current near the middle DW 3 (Fig. 5.12). However, DW 1- 4 all move as magnetic moments rotate to align with the local fields, indicated by the green lines in the graph. At the end of simulations, DW 1 diminishes at the left end while DW 2 moves close to the top left corner where DW 1 originally resides. DW 3 moves close the bottom left corner where DW 2 originally rests. DW 4 moves slightly to the left. DW 5 is not affected by the applied field. This final state is stable in a 0 field. For curved nanowires, the initial states resemble those of the zigzag nanowires,which are characterized by a series of alternating 180° DWs. However, as multiple DWs move together and do not combine, no 360° DWs are formed. Nonetheless, in a real sample, pinning at other DWs might lead to the formation of 360° DWs.

Although we treat the magnetic field around the AFM tip as a local field, it has a $1/r$ falloff (Equation 2.1) and therefore is felt over some distance away from the tip, thus affecting multiple DWs. This effectively proves that it is indeed easier to move DWs in curved structures because fields near DW 1 , 2 and 4 are much smaller than 25 mA, which is the minimal field required to move DWs in zigzag nanowires.

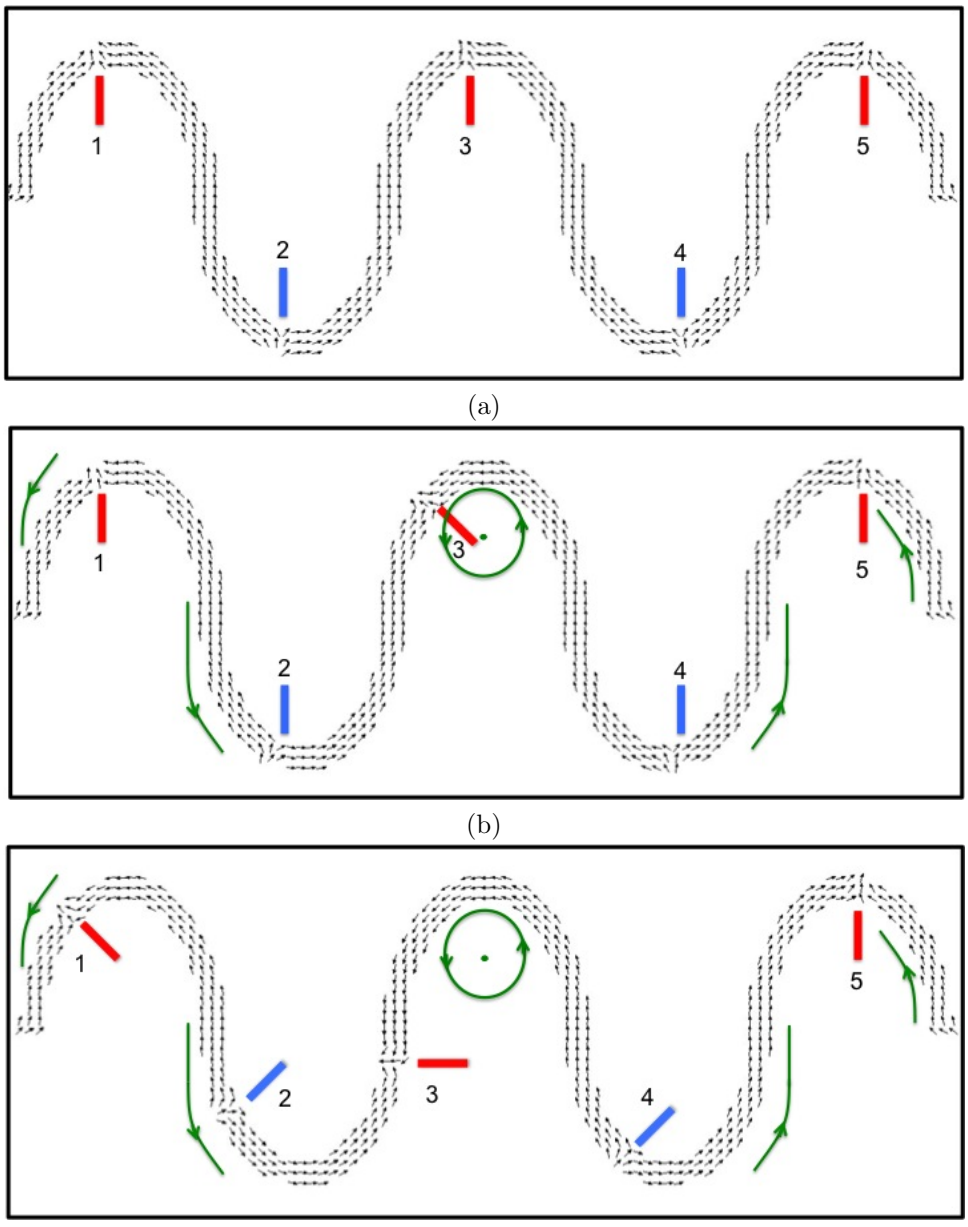

Figure 5.12

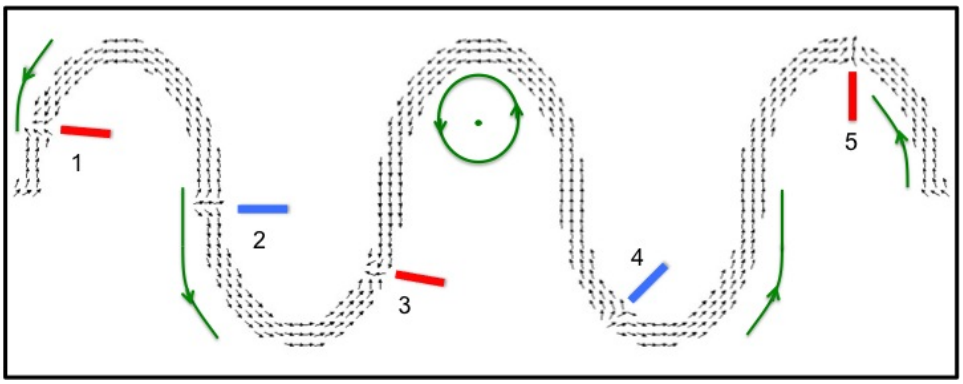

(d)

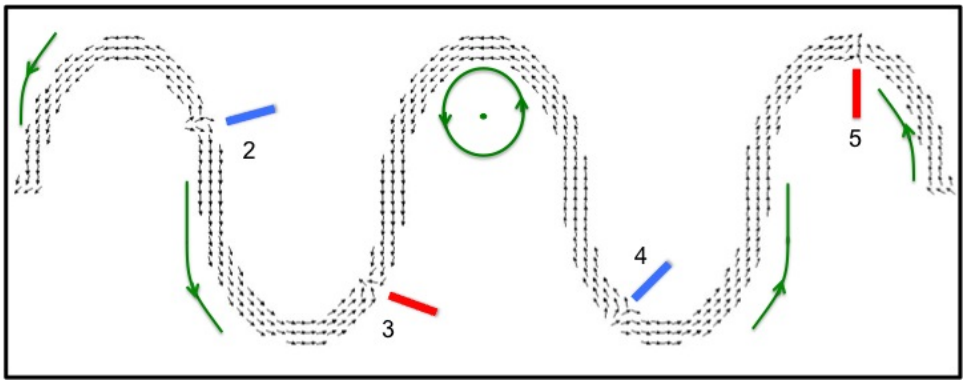

(e)

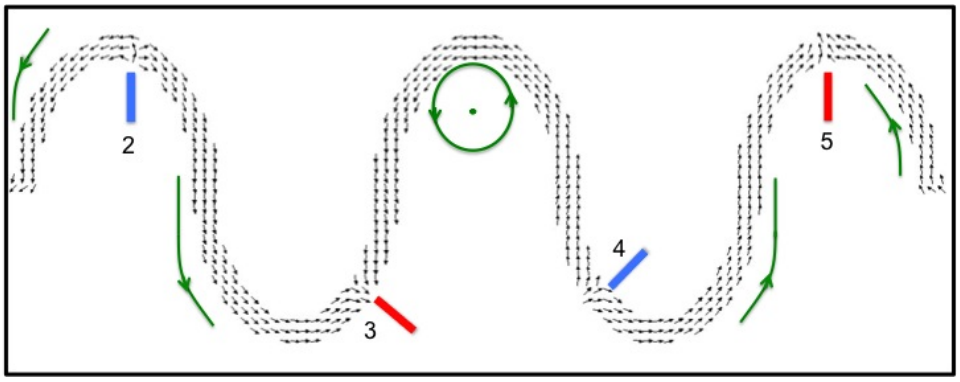

(f)

Figure 5.12: (a)-(c) DWs 1-4 move so that the moments are alined with local magnetic fields. (d)-(f) DW 1 diminishes at the left end; DW 2 moves to the top left arch; DW 3 and 4 are near the bottom arches; there is no DW in the top middle arch.

5.2.2 Experiment

Although simulation indicates no 360° DW, we do expect movement of 180° DWs. However, we have not observed DW motion after passing current near the DWs. The magnetization of nanowires stay the same before and after currents up to 120 mA are passed (Fig. 5.14). Fig. 5.13 shows the topography image of a typical curved nanowire sample and Fig. 5.14 shows the typical MFM image before and after currents are passed.

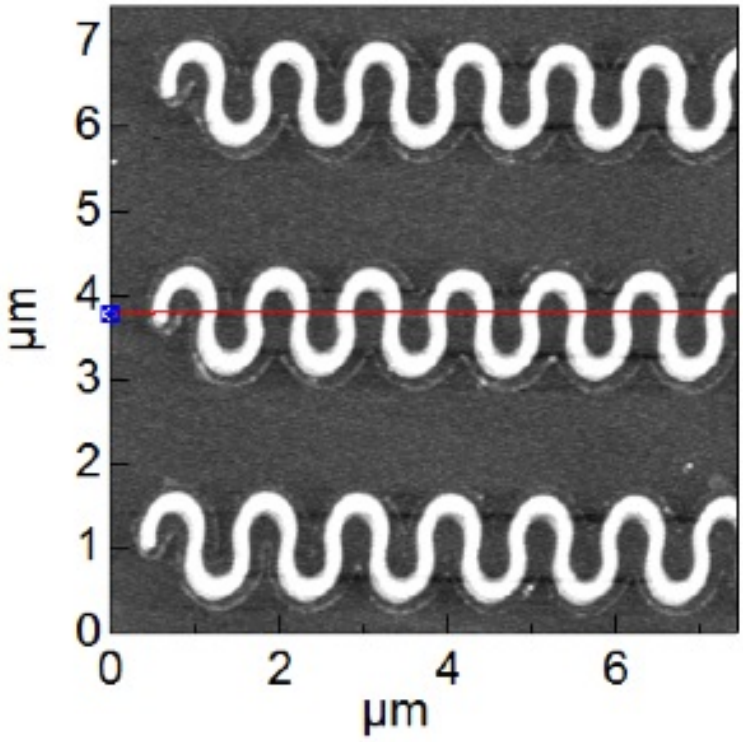

(a)

Figure 5.13

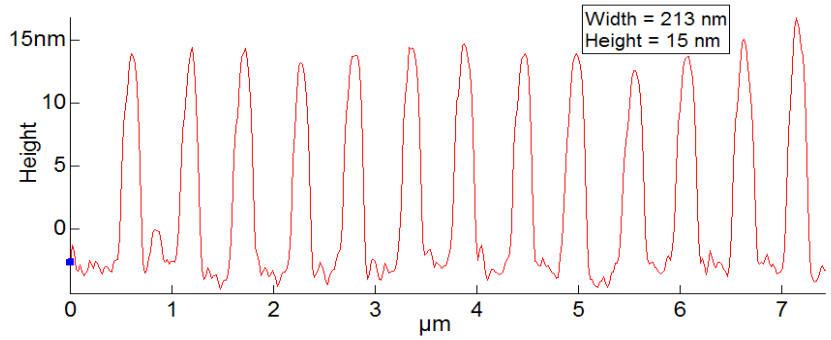

(b)

Figure 5.13: (a) top-down topography image of curved nanowires; (b) cross-sectional height profile of the sample along the red line in (a).

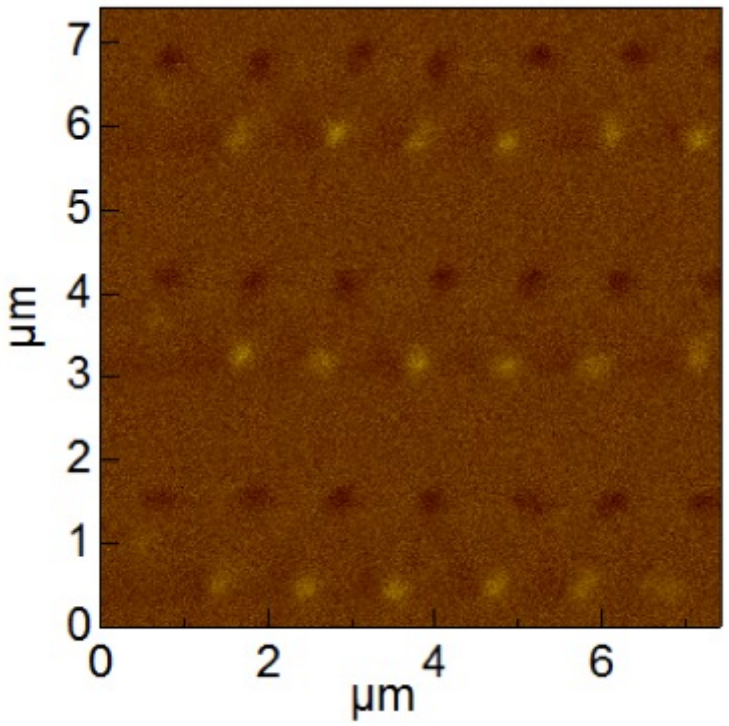

Figure 5.14: MFM image of curved nanowires. It does not change after currents are applied near the 180° DWs.

Although we have not moved DWs by applying currents, we have observed interesting states in curved nanowires. Fig. 5.15 shows a MFM image of a nanowire sample where several 180° DWs are close to each other, potentially forming 360° DWs. This image is obtained after currents are passed and the sample is left in the vacuum box overnight. No change is seen right after currents are passed so this state is probably unrelated to the local fields that we have applied.

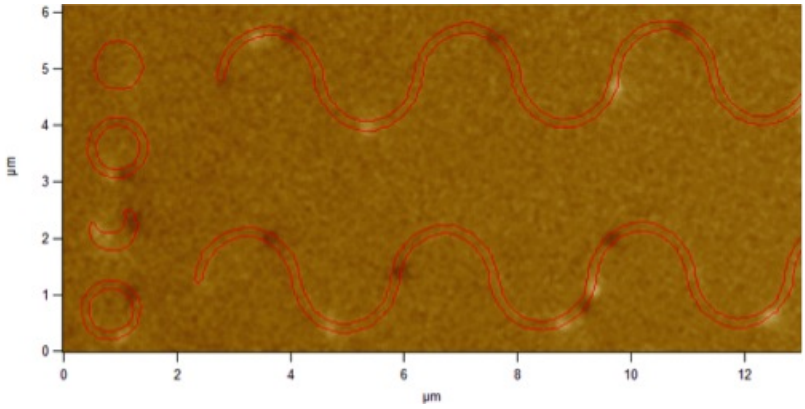

Figure 5.15: MFM image of two nanowires after currents are passed. No change is observed right after the current passing process, but DWs move around after the sample is left for a night.

5.3 Notched Nanowires

We examine the notched nanowire as it is a potential candidate of realizing racetrack memories. By passing spin-polarized currents, DWs in notched nanowires are possible to move. We conduct simulations and experiments to investigate if we can control DWs in notched wires by applying local fields via AFM tip.

5.3.1 Simulation

Simulations are performed with a straight nanowire with 2 notches. We saturate the wire in a field in the y-direction, decreases to a 0 field and increases the field in the -y-direction. Unlike zigzag nanowires or curved nanowires, we do not observe apparent DW formation in the wire (Fig. 5.16). This may be due to that the formation and propagation of DW is too fast to capture. The wire has a height of 10 nm and a width of 400 nm. Notches have widths of 200 nm and are 2000 nm apart.

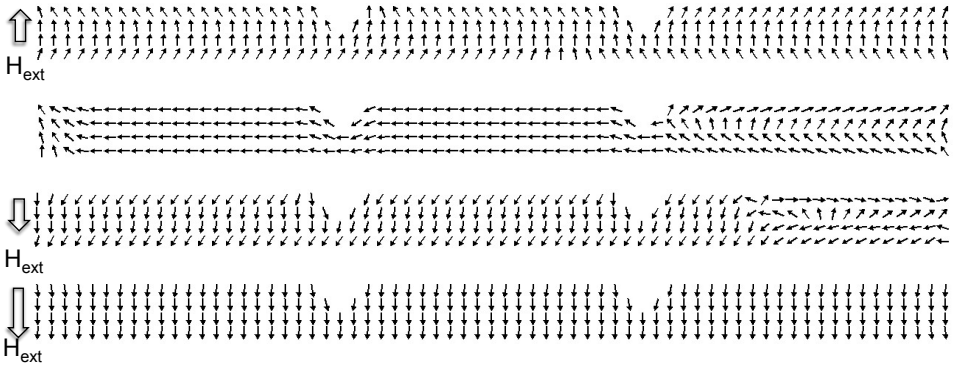

Figure 5.16: Evolution of micromagnetic configuration of a notched nanowire in the in-plane field in the y-direction.

We choose the remanent state at 0 field to begin with. We attempt to inject DW in the structures by applying current near the notch(Fig. 5.17).

Magnetic moments around where the current is passed deform and form a DW, but this DW is unstable in the 0 field.

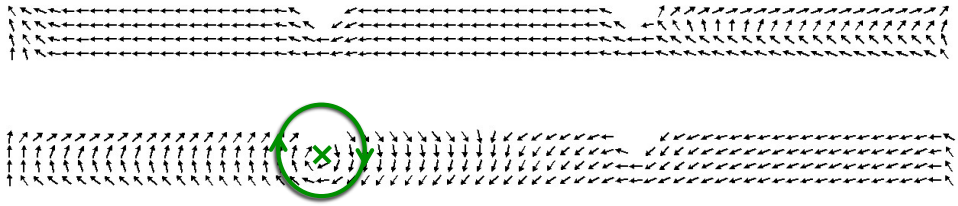

Figure 5.17: DW injection near the notch.

5.3.2 Experiment

We have fabricated notched nanowires with EBL (Fig. 5.18). On the contrary to simulations, notched wires exhibit complex DW structures at the remanent state, which is consistent to experimental results of other groups. We can see DWs near the notches, as they are designed as pinning sites. We can also see many DWs in the middle of arms, probably due to defects. However, we cannot move DWs by applying currents near the notches or in the middle between two notches (Fig. 5.19).

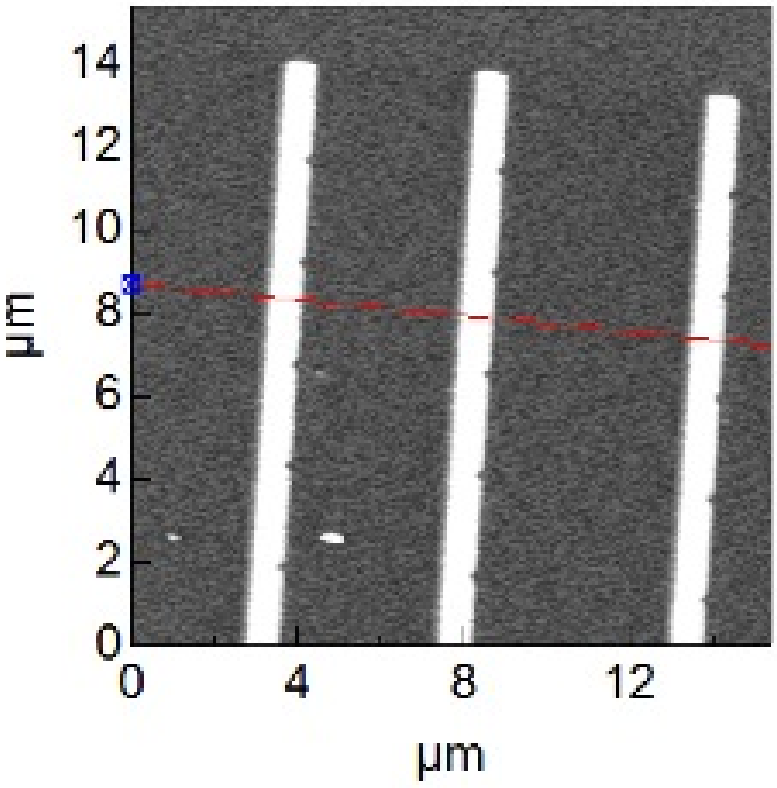

(a)

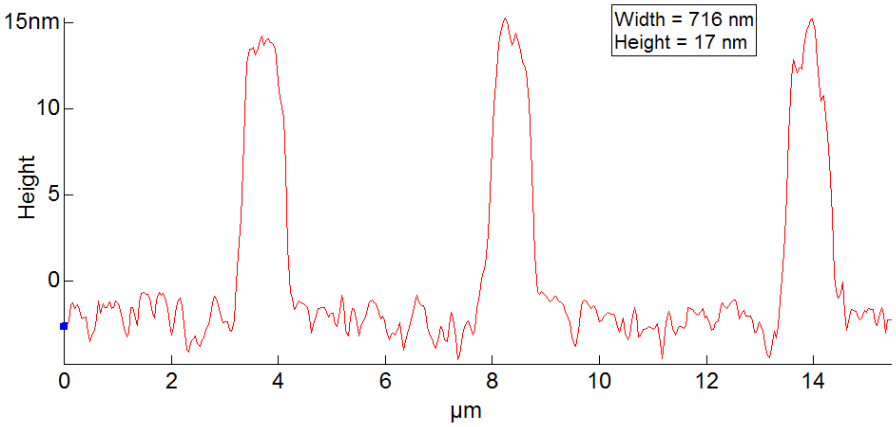

(b)

Figure 5.18: (a) top-down topography image of notched nanowires; (b) cross-sectional height profile of the sample along the redline in (a).

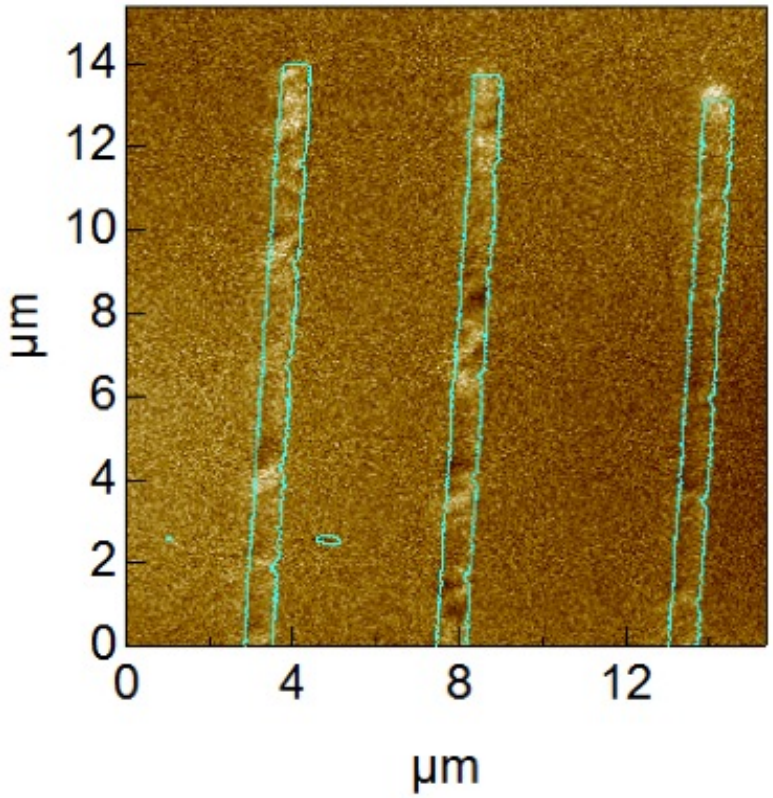

Figure 5.19: MFM image of notched nanowires. It does not change after currents are applied near the notches.

In this chapter, I summarized the simulation and experimental work performed on various nanowires. Simulations predict that DW motion is possible with localized circular fields. However, we are still in the working process to implement these motions in experiments. Various reasons can contribute to the discrepancy between simulations and experiments, and I will explore some in the next chapter.

6. Discussion and Conclusion

In this chapter, I will explore some possible reasons of the mismatch between simulation predictions and experimental measurements. Once we solve the involved problems and are able to move DWs in a controlled manner, we would like to explore the stochastic nature of DW motion and perform magnetoresistance measurements with our structures. These future studies will reveal the deeper physics of dynamic DW motion. I will provide a conclusion of this project in the end.

6.1 Practical Considerations

In this section, I will discuss practical concerns arising in fabrication, imaging and simulation process. Unlike the ideal condition in simulations, we deal with various defects in magnetic structures which inhibit DW motions. The way we carry out experimental and simulation procedures may also affect the result that we observe.

6.1.1 Sample Fabrication

Samples are not perfect: the surface is rough and it disturbs the magnetic structure and creates random pinning sites other than the intended ones. The pinning sites may strongly inhibit the DW motion. In addition, although we are capable of making structures as thin as 6 nm, our samples are usually around 15 nm to allow for detectable MFM signals. Micromagnetic structures vary greatly in samples with different thicknesses, complicating DM manipulations.

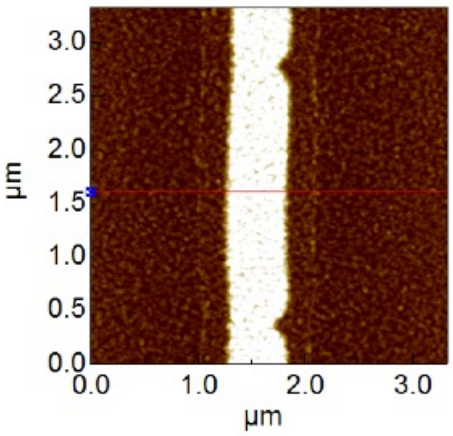

(a)

Figure 6.1

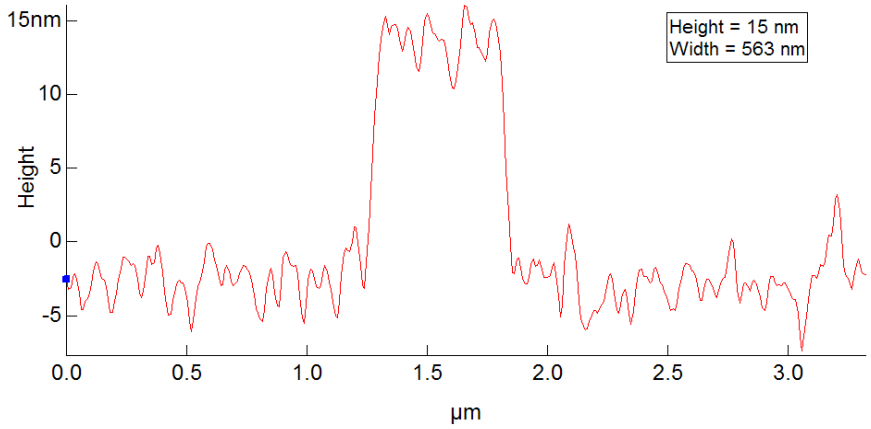

(b)

Figure 6.1: (a) top-down topography image of curved nanowires; (b) cross-sectional height profile of the sample along the redline in (a).

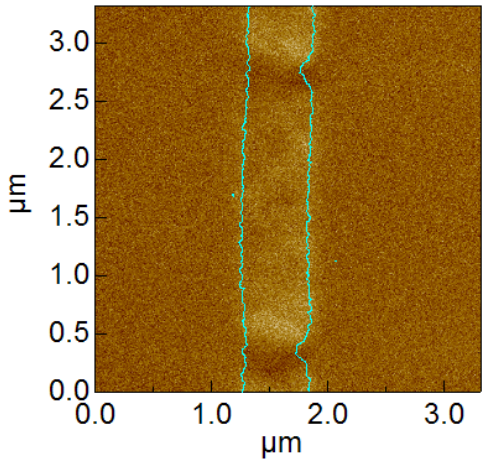

Figure 6.2: Zoomed-in MFM image of a typical notched wire sample.

Take a notched nanowire for example. Fig. 6.1 shows the topography image and cross sectional height profile along the red line. The height profile is rather ragged, showing an uneven surface. Although the MFM image (Fig. 6.2) shows no extra DW near the rough region, it is possible that rough surface or other defects lead to the irregular DW structures in Fig. 5.12.

In addition to defects, our measurements differ from the simulations

in terms of temperature. Simulations are performed with $0K$ while experiments are done in room temperature. Previous research points out that there are energy barriers that thermal energy can overcome, and it is difficult to predict exactly what DW will move at what applied field . These real-life factors complicate experiments greatly.

6.1.2 Applying Currents at Multiple Locations in Sequence

In simulation, we apply a current at one spot near the wire. In practice, however, we apply currents in a series of spots near the wires, as it is time consuming to detect stable MFM signals and it is inefficient to scan just one section of wire per image. This procedure may be problematic if successive currents have counter-effects at moving DWs. DWs may move to different locations due to the first current, but they may move back due to the second current. Or it is possible that DWs indeed move, but we cannot image the motion. For example, DW 2 and 3 move to the corners where DW 1 and 2 start, the MFM images for those two corners would be very similar before and after a current is passed(Fig. 5.12). We would not image that small a portion in experiments, so we can definitely see that there is no DW in the corner where DW 3 starts. However, passing currents at a series of locations may move the DWs in a way that we cannot tell any difference in MFM images. Simulations are performed on curved nanowires to explore that possibility.

Fig. 6.3 shows that DWs move again after the second current is passed. But we would still be able to image the difference as DW 5 moves away from its original position. Therefore, DWs are affected by magnetic fields each time after currents are passed, but theoretically we should be

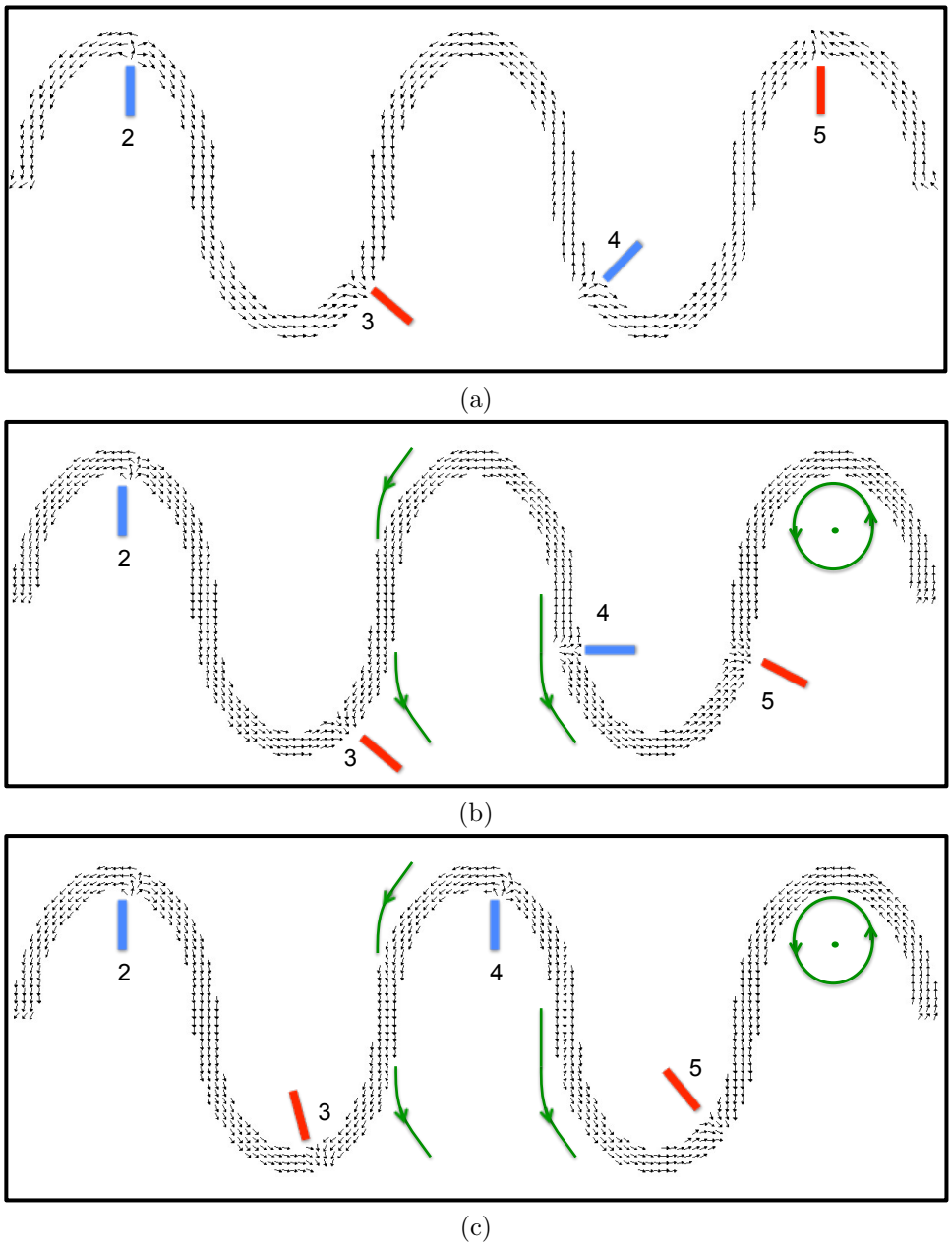

Figure 6.3: (a) Initial state where 25 mA current has been passed near the middle top corner. (b)-(c) DWs move after the current is passed to the top right corner.Eventually DW 4 moves to the top middle corner, DW5 moves to bottom left corner.

able to visualize that as the DW closest to the last current always moves away and no DW comes to its original position.

6.1.3 Cell Size Consideration

As discussed in chapter 3, we use OOMMF to simulate the cell-wise magnetization of samples. In practice, simulations with a large cell size run much faster than those with a small cell size. Therefore, at the beginning of searching through different geometries and passing currents at various locations, I use a xy cell size of 10×10 nm, and the size at z direction is usually the sample's height. Later, I switch to a smaller cell size, 4×4 nm. 4 nm is close to the exchange length of magnetic material and this cell size is widely used. Some research groups get similar results for both cell sizes [15]. But the two cell sizes produce different results for zigzag nanowires.

For a zigzag wire with the large cell size, simulations show that we can move a 180° DW to its neighboring vertex and form a 360° DW there. However, in simulations with the small cell size, no 360° DW ever forms. By passing a current once as in Fig. 5.3 (b), we get a result similar to Fig. 5.5 (b). The 360° DW is not stable even when the height is reduced to 5 nm.

Results for the two cell sizes are different, but the bottom line is that we have moved the 180° DW in both scenarios. With or without a 360° DW, we should be able to image the magnetization change before and after a current is passed. Also, there are many random pinning sites in the sample in reality, which may help to trap 180° DWs and form 360° DWs.

6.2 Stochastic Domain Wall Motion

Recent studies on curved nanowires and notched nanowires show that the strength of depinning fields and DW velocities are stochastic in nature, for both applying spin-polarized currents and applying in-plane magnetic fields[10, 11].By "stochastic" I mean that the DW is continuously pinned and depinned at the trapping sites, and the ultimate pinning or depinning is probabilistic. Once we develop a successful technique to move DWs, we can perform a careful study of this stochastic nature of pinning.

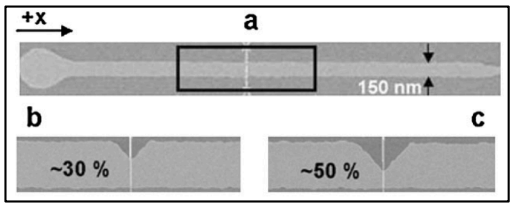

Figure 6.4: Samples to study field-driven depinning of DW trapped at a notch [10].

I will introduce an investigation of depinning fields of notched wire as an example here[10]. A wire with a notch in the middle is connected to a round pad on its left. (Fig. 6.4). The Eiselt group first applies field of 100 mT along the longitudinal axis of the wire in the +x-direction, and then gradually decreases the field to 0, and increase field in the -x-direction. As field switches, a DW generated from the round pad moves along the wire to the notch, and the field required to move the DW away from the notch is the depinning field. Wires are made with widths 150 nm, 250 nm and 450 nm. The depth of the notch (N_d) is 50% of the total width of the wire. For 250 nm width wire, N_d of 30% wire is also made. For each type of wire, identical measurements are repeated at least 40 times.

Fig. 6.5 shows the distribution of depinning fields for four types of

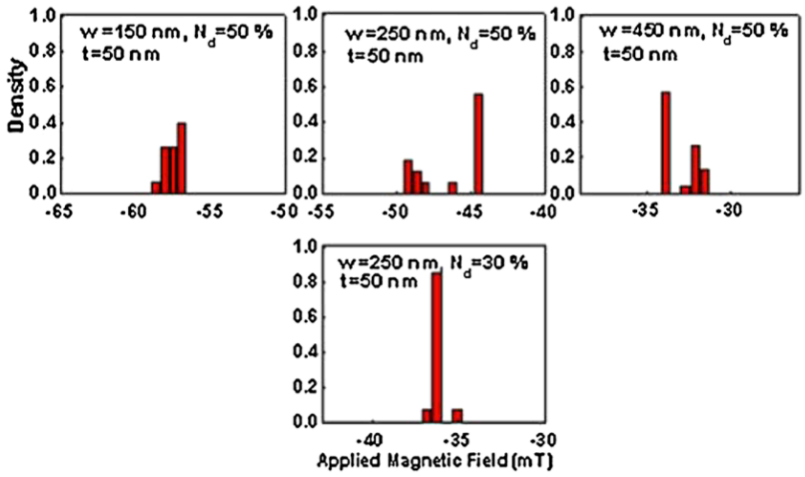

Figure 6.5: Depinning field distribution for each type of notched wires. The wires are 50 nm thick [10].

wires to investigate the correlation between depinning fields, wire width and notch depth. It is found that as wire width increases, the depinning fields in general decreases. The distribution of depinning fields also depends on wire geometries. The distribution for 250 nm wire is much broader than that of 150 nm and 450 nm wire. For 250 nm wire, the distribution shrinks as the notch depth decreases from 50% to 30%. It is argued that the stochastic nature of depinning field arises from the various DW types around the notch. Thermal activation is not the major contribution, because Gaussian distribution instead of isolated peaks is expected for thermally activated DW depinning.

We can see that the depinning fields for a single structure vary within 5 mA (Fig. 6.5). Therefore, it may be irrelevant to the large discrepancy between the simulation and experiments. Nevertheless, the stochastic nature increases the difficulty to manipulate DWs as the actual depinning fields will vary with the micromagnetic configuration in and around the DWs. Once we are able to manipulate DWs reliably, we can individually address the DWs and directly measure the variation.

6.3 Magnetoresistance Measurement

Mentioned in section 2.2, magnetic material displays magnetoresistance (MR) , as its electric resistance changes with its magnetic configuration. Magnetoresistance of wires has been studied extensively for their applications in read head, the device that hard drive uses to read data ([16, 17, 18]). In the future, we would like to measure the magnetoresistance of nanowires while manipulating DWs. Instead of relying on the images of wires' stable magnetic states after currents are passed, we will be monitoring the live change of wires electric resistances. In order to measure the resistance, we will be passing currents through wires. These currents through the wires may lead to DW deformation and movement as discussed in chapter 2. But we will pass currents below a certain threshold to make sure that DWs only respond to the applied magnetic fields. The MR measurement will reveal more details for the real-time DW motion and interactions, and will help us to better understand DWs.

6.4 Conclusion

Domain walls have potential applications and they have been studied extensively in various structures. For this project, we mainly explore three types of ferromagnetic structures: zigzag, curved and notched nanowires. We explore the motion and interaction of individual DWs by applying local circular fields with the AFM tip. Both simulation and experimental methods are employed.

Simulations show that it is possible to form, separate and annihilate 360° DWs in zigzag nanowires. Multiple DW movements are observed in simulations for curved nanowires. Although simulations for notched nanowires are inconclusive, they display complicated DW structures in experiments.

We are currently working on to experimentally implement DW motion with the AFM tip. Many practical problems arise in experiments during fabrication and imaging. We are dealing with inhomogeneous and thick samples at room temperatures. Nevertheless, we are searching new geometries and improving sample quality. Once we successfully manipulate individual DWs, we would like to carry out real time measurement on the stochastic behavior of DW pinning and magnetoresistance of DWs in multilayers. These future measurements will reveal physics of domain wall dynamics at greater depth.

A. Procedures to Apply Local Fields

In this appendix, I will introduce the step-by-step procedure of applying local magnetic fields by passing current through the AFM tip. We start with connecting the circuit of AFM and the resistor. We then scan a regular topography image of the sample to determine where to pass currents. After that, we would compile required files and adjust settings in the built-in program of the AFM. The AFM machine will apply a voltage, and therefore passing a current through the AFM tip.

1. Connect the sample with the 40 Ω resistor. The resistor is hooked to a T connector, one goes to the ground, the other goes to the BNC channel 0 of the AFM controller box. Mount the conductive Pt tip onto the mount stage of AFM. When the tip is in contact the sample, a complete circuit forms (Fig. A.1). The cantilever has a conductive pad connected to the tip, it is critical to make sure the pad is in good contact with the metal clamp of the mount stage, so that the tip is connected to the AFM machine.

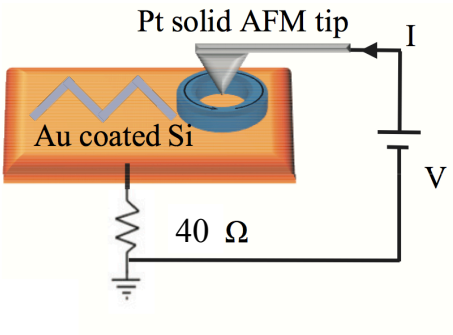

Figure A.1: Adjust imaging mode of AFM.

2. Scan the topography image of the sample with the Pt tip to find the desired locations to pass currents. Use AC mode to avoid damage to

the sample or the tip (Fig. A.2). Go to Master Panel → Main, select AC in the imaging mode.

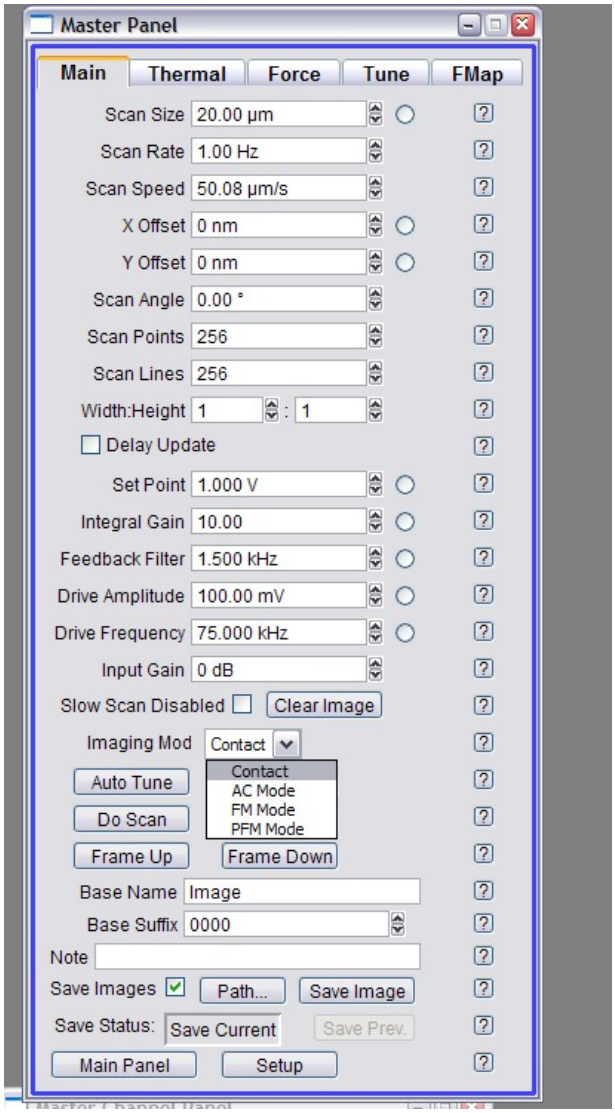

Figure A.2: Adjust imaging mode of AFM.

3. Load the procedure file to pass currents. Go to the menu: File → open file → procedure. Find DoIV3.ipf file in the folder 2009 → 0616 → KA. Compile the file. This file enables the AFM to apply voltage to the tip and calculate the resulting current.

4. Adjust the program so that it will display the live voltage across the

tip via channel 0. Click the setup button on the "Sum and Deflection Meter" panel, select "Tip Bias" and "User 0".

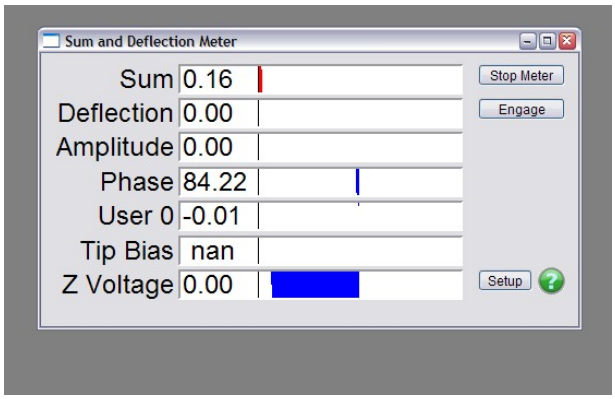

Figure A.3: Bring up the tip voltage.

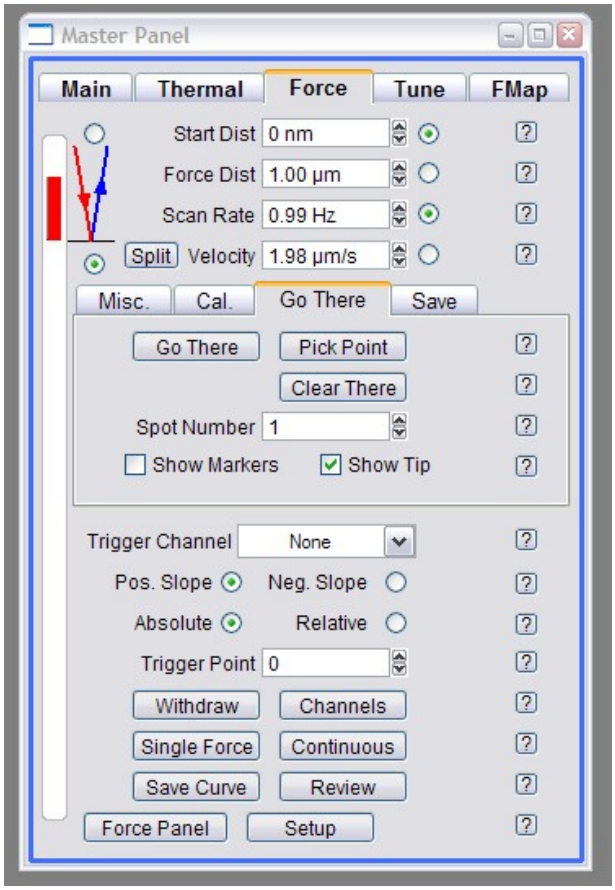

Figure A.4: Select the location to pass current.

5. Connect the tip on the right position of the sample. Go to Mas-

ter Panel → Main, select Contact in the imaging mode. Therefore, the tip switches from the AC mode and can touch the sample (Fig. A.2). Go to Master Panel → Force → Go there and select Show tip (Fig. A.4). In this way, the topography AFM image will show the current tip position. Click Pick Point so the image will display a curser which we can drag to change the tip position. Once we find the right location, click Go There and the tip will go to that new position. Go to the Sum and Deflection Meter panel and click Engage. In this way, the sample is brought to firm contact with the sample at the desired location.

6. Input the circuit circuit structure to AFM. Go to the menu: Programming → Crosspoint Panel (Fig. A.5). Set InA to BNCIN0, InB to ground, and Chip to OutC. Click Write Crosspoint. This effectively tells the AFM machine to apply a voltage wave through BNC channel 0, to which the resistor is connected.

7. We are now ready to apply voltage waves through AFM tip. Start with a small voltage to test the electric connection. Type td_writevalue ("C% Output", 0.5) in the command prompt. This puts 0.5 V on the tip and we should see it at the Tip Bias in the Sum and Deflection Meter. We should see some value in the User 1 as well if the electric connection is reliable. We then apply the actual voltage wave to the tip. Type DOIV3(0, 4.0, 0.5) in the command prompt. The first number is the starting voltage, the second is the ending voltage, and the third is the rate. This corresponds to roughly 100 mA through the tip. Uncheck Engage in the Sum and Deflection Meter immediately to bring the tip up away from the sample to avoid excessive heating in the tip and sample.

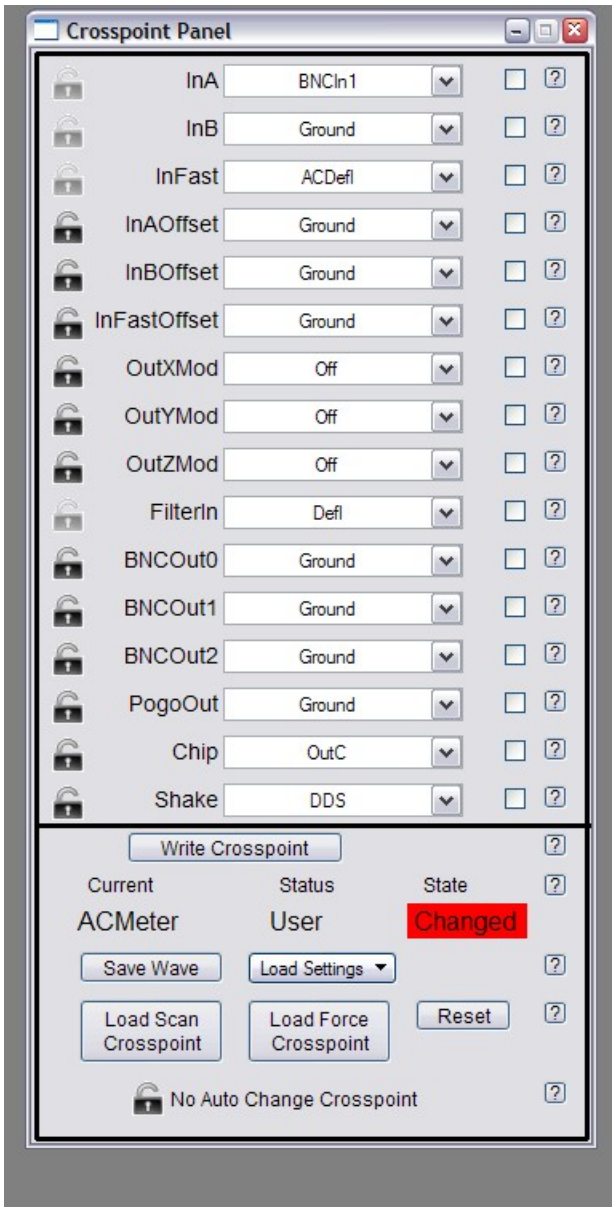

Figure A.5: Adjust the crosspoint setting.

8. Display the IV curve to check if current has been passed successfully. Go to Windows → New Graph, and select CurrentWave as the y axis and VoltageWave as the axis. Fig. A.6 shows an IV curve where the current is passed nicely through the tip.

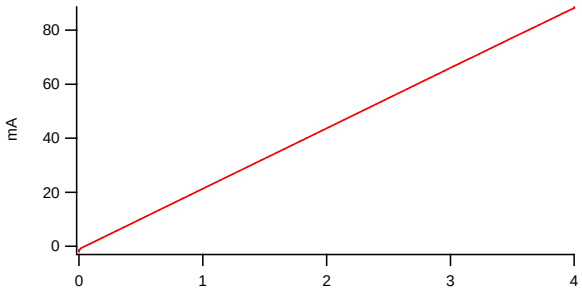

Figure A.6: The IV curve of a successful current passing.

9. Repeat steps (5)-(8) to apply currents at different locations in a series. After that, switch back to AC mode in the Main menu.

Bibliography

[1] N. R. Pradhan, A. S. Licht, Y. Li, Y. Sun, M. T. Tuominen, and K. E. Aidala, "Switching of ± 360° domain wall states in a nanoring by an azimuthal oersted field," *Nanotechnology*, vol. 22, no. 48, 2011.

[2] T. Yang, N. R. Pradhan, A. Goldman, A. S. Licht, Y. Li, M. Kemei, M. T. Tuominen, and K. E. Aidala, "Manipulation of magnetization states of ferromagnetic nanorings by an applied azimuthal oersted field," *Applied Physics Letters*, vol. 98, no. 242505, 2011.

[3] S. S. Parkin, M. Hayashi, and L. Thomas, "Magnetic domain-wall racetrack memory," *Science*, vol. 320, p. 190, 2008.

[4] C.-Y. You, "Concept of the field-driven domain wall motion memory," *Journal of Magnetism and Magnetic Materials*, vol. 321, no. 888, 2009.

[5] "Fabrication techniques," *http://wwwold.ece.utep.edu/research/webedl/cdte/Fabrication/*.

[6] P. Rai-Choudhury, *Handbook of Microlithography*, vol. 1. Institution of Engineering and Technology (IET), 1997.

[7] C. R. Blanchard, "Atomic force microscopy," *The Chemical Educator*, vol. 1, no. 5, 1996.

[8] S.-W. Jung, W. Kim, T.-D. Lee, K.-J. Lee, and H.-W. Lee, "Current-induced domain wall motion in a nanowire with perpendicular current-induced domain wall motion in a nanowire with perpendicular magnetic anisotropy," *Applied Physics Letters*, vol. 92, no. 202508, 2008.

[9] V. Uhlír, S. Pizzini, N. Rougemaille, J. Novotny, V. Cros, E. Jiménez, G. F. Heyne, F. Sirotti, C. Tieg, A. Bendounan, F. Maccherozzi,

R. Belkhou, J. Grollier, A. Anane, and J. Vogel, "Current-induced motion and pinning of domain walls in spin-valve nanowires studied by xmcd-peem," *Physical Review B*, vol. 81, no. 224418, 2010.

[10] G. Meier, M. Bolte, and R. Eiselt, "Direct imaging of stochastic domain-wall motion driven by nanosecond current pulses," *Physical Review Letters*, vol. 98, no. 187202, 2007.

[11] M.-Y. Im, L. Bocklage, P. Fischer, and G. Meier, "Direct observation of stochastic domain-wall depinning in magnetic nanowires," *Physical Review Letters*, vol. 102, no. 147204, 2009.

[12] M. J. Donahue and D. G. Porter, *OOMMF User's Guide, Version 1.0*. Interagency Report NISTIR 6376, National Institute of Standards and Technology, Geithersburg, MD, September 1999.

[13] M. Lakshmanan, "The fascinating world of landau-lifshitz-gilbert equation: An overview," *Philosophical Transactions of the Royal Society A*, January 2011.

[14] A. S. Licht, *A Computational Micromagnetic Study of Controlling Vortex Chirality in Ferromagnetic Nanorings*. Mount Holyoke College, May 2011.

[15] N. Dao and S. L. Whittenburg, "Micromagnetic simulation of deep-submicron supermalloy disks," *Journal of Applied Physics*, vol. 90, January 2001.

[16] D. Buntinx, S. Veleman, A. Volodin, and C. V. Haesendonck, "Ferromagnetic domain configuration and electrical resistance of co zigzag wires," *Journal of Magnetism and Magnetic Materials*, vol. 242, p. 1257, April 2002.

[17] T. Koyama, G. Yamada, H. Tanigawa, S. Kasai, N. Ohshima, S. Fukami, N. Ishiwata, Y. Nakatani, and T. Ono, "Control of domain wall position by electrical current in structured co/ni wire with perpendicular magnetic anisotropy," *Applied Physics Express*, October 2008.

[18] C. Boone, J. Katine, M. Carey, J. R. Childress, X. Cheng, and I. N. Krivorotov, "Rapid domain wall motion in permalloy nanowires excited by a spin-polarized current applied perpendicular to nanowires," *Physical Review Letters*, vol. 104, no. 097203, 2010.

[19] J. Shibata, G. Tatara, and H. Kohno, "A brief review of field- and current-driven domain-wall motion," *Journal of Physics D: Applied Physics*, vol. 44, no. 38, 2011.

[20] D. Rugar and P. Hansma, "Atomic force microscopy," *Physics Today*, p. 23, October 1990.

[21] G. E. Llyod, "Atomic number and crystallographic contrast images with the sem: a review of backscattered electron techniques," *Mineralogical Magazine*, vol. 51, p. 3, March 1987.

[22] D. A. Allwood, G. Xiong, C. C. Faulkner, D. Atkinson, D. Petit, and R. P. Cowburn, "Magnetic domain-wall logic," *Science*, vol. 309, p. 1688, 2005.

[23] U. Hartmann, "Magnetic force microscopy," *Annual Review of Material Science*, vol. 29, p. 53, 1999.

[24] D. Rugar, H. J. Mamin, P. Guethner, S. E. Lambert, J. E. Stern, I. McFadyen, and T. Yogi, "Magnetic force microscopy: General principles

and application to longitudinal recording media," *Journal of Applied Physics*, vol. 68, August 1990.

[25] T. Manago, K. Kanazawa, and T. Kera, "Magneto-resistance of nife nanowire with zigzag shape," *Journal of Magnetism and Magnetic Materials*, vol. 321, p. 2327, 2009.

[26] J. M. D. Coey, *Magnetism and Magnetic Materials*. Cambridge University Press, April 2010.